

Strain-Controlled Magnetic Phase Transitions through Anisotropic Exchange Interactions: A Combined DFT and Monte Carlo Study

Sudip Mandal,¹ Mihir Ranjan Sahoo,² and Kalpataru Pradhan¹

¹ *Theory Division, Saha Institute of Nuclear Physics,
A CI of Homi Bhabha National Institute, Kolkata 700064, India*

² *Graz University of Technology, 8010 Graz, Austria*

(Dated: December 19, 2025)

Epitaxial strain provides a powerful, non-chemical route to tune the properties of functional materials by manipulating the coupling between spin, charge, and lattice degrees of freedom. Using density functional theory (DFT) calculations and BiFeO_3 as a model system, we first demonstrate how epitaxial strain exactly leads to anisotropic magnetic interactions where the exchange coupling along the c -axis differs from that in the ab -plane. We show that subtle structural modifications, specifically the distortion from a cubic to a tetragonal lattice, drive a magnetic phase transition from a G-type to a C-type antiferromagnetic (AF) phase. The anisotropy in magnetic interactions, which becomes prominent in the lower symmetry tetragonal phase, provides a direct link between the structural distortion and the potential change in magnetic ordering. For a more comprehensive study, we next investigate the role of strain in driving magnetic phase transitions within a half-filled one-band Hubbard model in three dimensions. In this framework, strain is introduced through anisotropic hopping processes between nearest- and next-nearest-neighbor sites, inspired by the DFT calculations. Using a semiclassical Monte Carlo (s-MC) approach, we construct ground state phase diagrams in the nonperturbative regime, which show how uniaxial strain stabilizes distinct magnetic ground states: Compressive strain drives a transition from a G-type to a C-type AF insulator, whereas tensile strain suppresses the C-type AF order, favoring an A-type AF phase. Overall, our combined DFT and s-MC calculations highlight that strain is a powerful tuning parameter for controlling competing magnetic phases by governing exchange coupling mechanisms in correlated systems, offering valuable insights for the design of strain-controlled materials.

I. INTRODUCTION

Competing spin interactions are central to the unusual properties of correlated materials in physics [1–4]. The interplay between these interactions often leads to novel and intriguing phenomena [5–7]. Interestingly, when the strengths of these interactions are nearly balanced, the system becomes extremely sensitive to small perturbations like temperature, pressure, or strain, resulting in complex, rich phase diagrams where minor changes can trigger transitions between different magnetic phases [8, 9]. This sensitivity is mostly due to the strong correspondence that exists between spin interactions and the crystal lattice. Since magnetic properties are intrinsically linked to the underlying structure, lattice distortions significantly influence magnetic behavior, directly altering exchange interactions and spin configurations [10, 11]. Therefore, alterations to the crystal structure can directly impact the magnetic ground state. Understanding these coupled structural and magnetic transitions is crucial for advancing condensed matter physics and exploring applications in new technologies.

Materials exhibiting magneto-structural transitions, in which magnetic and lattice degrees of freedom are strongly coupled, are of considerable interest from both fundamental and applied viewpoints [12, 13]. On the fundamental side, such transitions offer a well-defined framework to investigate how lattice symmetry breaking influences the magnetic ordering, electronic correlations, and exchange interactions, thereby providing valuable in-

sights into the physics of correlated electron systems. From an applied perspective, this strong coupling enables external control of the magnetic states through strain, pressure, or temperature. This tunability is particularly promising for spintronic and memory applications, where switching between distinct magnetic states via structural modulation can enable energy-efficient, non-volatile device operation [14]. A detailed understanding of these coupled magnetic and structural transitions is therefore crucial for advancing both fundamental condensed matter physics and functional material design.

The close connection between the lattice structure and the magnetism is clearly apparent in perovskite oxides, where chemical substitution typically causes simultaneous structural and magnetic transformations [15–17]. When a few of the ions are replaced by others of differing size or charge, the resulting chemical pressure introduces internal strain, distorting the crystal structure to accommodate the modified bonding [18, 19]. These lattice distortions consequently alter inter-atomic distances and bond angles, directly tuning the superexchange pathways that govern magnetic ordering. A key example is $\text{Sr}_{1-x}\text{Ba}_x\text{MnO}_3$, where substituting Ba for Sr causes a progressive tetragonal distortion that strongly impacts the magnetic ground state [20, 21]. At low Ba content, the nearly cubic phase exhibits a G-type antiferromagnetic (AF) order. However, as the Ba concentration rises, the increasing tetragonal distortion drives the system away from pure G-type AF order, initially resulting in a mixed antiferromagnetic-ferromagnetic phase before

finally stabilizing a pure ferromagnetic (FM) order. Another significant illustration is $\text{La}_{0.2}\text{Sr}_{0.8}\text{MnO}_3$ [22–25]. This material has a nominally cubic perovskite structure and is paramagnetic (PM) above room temperature, however local MnO_6 octahedral distortions are already present. Upon cooling, it undergoes a dramatic magneto-structural transition into a tetragonally distorted phase, which is intimately associated with the emergence of C-type AF ordering.

The same underlying principle—that lattice distortions induced by ionic-size mismatch can dictate magnetic ordering—is also evident in other Mn-based perovskites such as CaMnO_3 and CdMnO_3 . Differences in the ionic radii of Ca and Cd lead to distinct lattice symmetries and, consequently, different magnetic ground states: CaMnO_3 crystallizes in an orthorhombic perovskite structure and exhibits G-type AF ordering with $T_N \approx 123$ K [26, 27], whereas CdMnO_3 , which incorporates the smaller Cd ion, is stabilized in a tetragonal perovskite lattice and displays a C-type AF ground state with a reduced $T_N \approx 86$ K [28].

Electronic instabilities, such as the Jahn–Teller effect, provide another route to structural distortion [29–31]. This effect, originating from the lifting of orbital degeneracies in transition metal ions with partially filled d orbitals, drives spontaneous lattice distortions that lower the electronic energy. In perovskites, these distortions typically manifest as elongations or compressions of the metal–oxygen octahedra, directly coupling orbital, lattice, and spin degrees of freedom. A notable example is LaMnO_3 , where cooperative Jahn–Teller distortions of Mn^{3+} ions stabilize an orthorhombic structure at room temperature, strongly influencing its A-type AF order [32]. The principle of electronic instability driving structural change is also evident in materials like LaCoO_3 , which undergoes a phase transition from a rhombohedral structure to a cubic lattice at temperatures above approximately 1200 K, a transition often linked to spin-state changes [33].

While structural changes are naturally induced by intrinsic factors like ionic-size mismatch and electronic instabilities (e.g., the Jahn–Teller effect), epitaxial strain is one of the most commonly used extrinsic tools to modify and control material properties by driving structural phase transitions, modifying electronic bandwidth, or affecting magnetic ordering [34–40]. Specifically, when a material is grown epitaxially on a substrate with a different lattice constant, the resulting lattice mismatch generates strain that distorts the unit cell and perturbs the orbital overlap and exchange interactions [41–43]. Hence, resulting strain can compress or elongate bond lengths and change bond angles, thereby tuning the strength and geometry of exchange interactions [44–51]. This directly affects key electronic parameters such as the hopping amplitudes and superexchange pathways, which are essential in determining the magnetic ground state [52, 53].

The power of epitaxial strain in modifying bond lengths and angles—and thus tuning electronic and mag-

netic behavior—is demonstrated across various material systems. An example of strain-controlled magnetism is found in the iridate Sr_2IrO_4 . While the bulk material shows a canted G-type AF order with Néel temperature $T_N \approx 240$ K [54], tensile strain enhances T_N , whereas compressive strain suppresses it [50, 55, 56]. This modulation of T_N is a direct result of strain-induced changes in the Ir–O–Ir bond angles. Similarly, EuTiO_3 , which in bulk crystallizes in a cubic perovskite structure and exhibits G-type AF ordering at low temperatures with $T_N \approx 5.6$ K [57–59], provides a demonstration of strain-driven transition. Under epitaxial strain, it undergoes a cubic-to-tetragonal distortion that weakens the AF superexchange and stabilizes a ferromagnetic order [60].

BiFeO_3 is another extensively studied example of a strain-induced magnetic transition; in this multiferroic material, strain can drive a transition between G-type and C-type AF orders [61–65]. In its pseudocubic structure, the dominant nearest-neighbor (NN) superexchange interactions are nearly isotropic, favoring G-type AF ordering. However, when strain lowers the crystal symmetry to tetragonal, the emergence of a distinct c axis introduces anisotropic exchange interactions. These anisotropies, together with the contribution of next-nearest-neighbor (NNN) couplings, can stabilize a C-type AF configuration. First-principles density functional theory (DFT) calculations have been instrumental in clarifying these mechanisms, providing insights into the electronic structure, total energies, and changes in magnetic exchange interactions across different structural phases. DFT studies on BiFeO_3 have explicitly demonstrated the strain-induced transition between C-type and G-type AF ordering, as well as its impact on band dispersion and optical properties [66–71]. Similar strain-controlled transitions have been reported in related perovskites, including BiCoO_3 [66, 68] and BiCrO_3 [69, 70], underscoring the broader role of strain in tuning magnetic phases. Even more intricate strain-driven phase behavior has been predicted in double perovskites: for instance, $\text{Ca}_2\text{FeOsO}_6$ transitions from a G-type ferrimagnetic phase to a C-type AF phase under compression, and further to an E-type AF phase under tensile strain [72], while $\text{Sr}_2\text{FeOsO}_6$ undergoes a C-type AF to G-type ferrimagnetic transition under epitaxial strain [73].

Such strain-induced symmetry lowering has profound consequences for both electronic and magnetic properties. It lifts degeneracies in the electronic band structure, alters the Fermi surface, and significantly influences transport behavior [39, 74]. Simultaneously, lattice distortions modify inter-atomic distances and bond angles—particularly those involving magnetic and non-magnetic ions such as oxygen—thereby tuning the superexchange interactions. Thus, these structural changes directly affect the strength and geometry of magnetic exchange, including both NN and NNN couplings [67, 68]. This control over symmetry and exchange interactions is highly versatile: the specific structural transition (like a cubic-to-tetragonal distortion) can itself be triggered not only

by epitaxial strain but also by other external or internal factors such as temperature, magnetic field, or chemical doping.

We aim to qualitatively understand the mechanisms that drive strain-induced magnetic phase transitions in correlated materials. To achieve this, we utilize the half-filled one-band Hubbard model [75–80] on a simple cubic lattice. Strain is modeled by introducing anisotropic hopping amplitudes—specifically, nearest-neighbor (t_x , t_y , t_z) and next-nearest-neighbor (t'_{xy} , t'_{yz} , t'_{xz}) terms. These directionally dependent hopping parameters essentially modify the electronic structure by modulating the effective bandwidth, shifting the Fermi level, and introducing magnetic frustration. Collectively, these changes destabilize conventional magnetic ordering, thereby paving the way for different kind of magnetic phases.

To explore the resulting electronic and magnetic properties, we systematically vary these hopping parameters and employ the semiclassical Monte Carlo (s-MC) technique [81–87] to map the evolution of the magnetic ground states. Our focus is on the non-perturbative regime, where the on-site repulsive Hubbard interaction (U) is comparable to the non-interacting electronic bandwidth. This regime is highly relevant for correlated materials, as it highlights the fundamental competition between electron mobility and Coulomb repulsion—the key interplay that dictates the emergence of new magnetic phases and transitions in such systems.

This paper is organized to first introduce the theoretical framework before discussing the results. We begin in Sec. II by presenting the DFT calculations used to estimate direction-dependent exchange couplings and establish the realistic model parameters for BiFeO_3 under epitaxial strain. In Sec. III, we define the anisotropic one-band Hubbard Hamiltonian and outline the s-MC framework used to study strain-driven magnetic and transport phenomena. Details regarding the derivation of the effective Hamiltonian and the numerical procedures for computing magnetotransport observables are provided in Appendix A and Appendix B, respectively. The results are then analyzed systematically: in Sec. IV, we examine the effect of compressive strain on magnetic ordering, while Sec. V extends the analysis to the tensile strain regime and reveals the associated reorganization of competing AF phases. Finally, the key results are summarized in Sec. VI.

II. ESTIMATION OF HOPPING PARAMETERS USING DFT

The magnetic transition, for example from G-type AF to C-type AF in BiFeO_3 , induced by strain, likely originates from a change in the dominant magnetic exchange pathways as the crystal structure evolves. In a cubic lattice, if AF interactions are the only dominant interactions, they are typically isotropic, favoring the G-type AF ordering where spins on neighboring sites are antiparallel

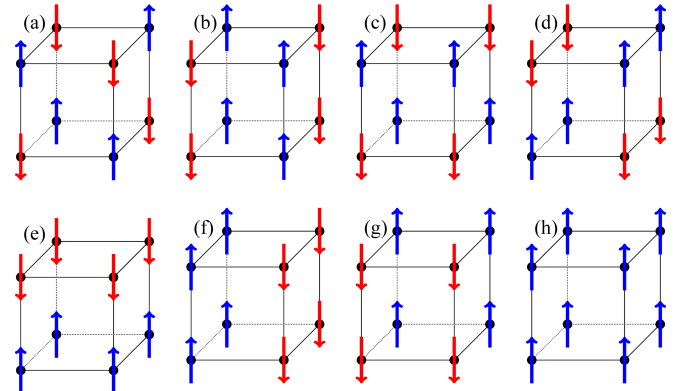


FIG. 1. Representative magnetic spin configurations on a simple cubic lattice, characterized by distinct ordering vectors \mathbf{q} . (a) G-type AF: spins alternate along all three spatial directions, $\mathbf{q} = (\pi, \pi, \pi)$. (b) C-type AF($\pi, \pi, 0$): AF order in the xy -planes with ferromagnetic stacking along z , $\mathbf{q} = (\pi, \pi, 0)$. (c) C-type AF($\pi, 0, \pi$): AF alignment in xz -planes with ferromagnetic coupling along y , $\mathbf{q} = (\pi, 0, \pi)$. (d) C-type AF($0, \pi, \pi$): AF alignment in yz -planes with ferromagnetic stacking along x , $\mathbf{q} = (0, \pi, \pi)$. (e) A-type AF($0, 0, \pi$): spins align ferromagnetically within each xy -plane, with neighboring planes stacked antiferromagnetically along the z -axis; $\mathbf{q} = (0, 0, \pi)$. (f) A-type AF($0, \pi, 0$): ferromagnetic alignment in the xz -plane, with alternating spin orientation along the y -axis; $\mathbf{q} = (0, \pi, 0)$. (g) A-type AF($\pi, 0, 0$): ferromagnetic layers lie in the yz -plane, coupled antiferromagnetically along the x -direction; $\mathbf{q} = (\pi, 0, 0)$. (h) FM: uniform spin alignment across the lattice, $\mathbf{q} = (0, 0, 0)$.

in all three dimensions. However, when the crystal structure transitions to tetragonal under strain, the symmetry is lowered, introducing a unique c -axis different in length from the a and b axes. This structural distortion leads to anisotropic exchange interactions, where the magnetic coupling strength becomes direction-dependent. These anisotropic interactions, possibly supplemented by the NNN exchange interactions, can then favor a C-type AF order in the tetragonal structure. Overall, the observed magnetic transitions are attributed to a complex interplay of factors, specifically the anisotropic exchange interactions and the competition between magnetic exchange pathways depending on the magnitude of the tetragonal distortion.

We begin by using DFT to extract realistic parameters for building a minimal model for studying the magnetic transitions in correlated materials under epitaxial strain. We use BiFeO_3 as a model system for our DFT calculations. Our goal is to connect the microscopic exchange couplings and eventually the hopping amplitudes to the strain-induced structural anisotropy, and thereby to identify the key parameters that control the competition between different magnetic orders. Please note that under epitaxial strain, the lattice parameters may evolve anisotropically, providing a route to tune the magnetic ground state. Representative magnetic spin configurations characterized by distinct ordering vectors \mathbf{q} are

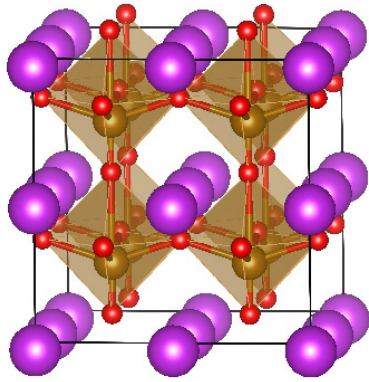


FIG. 2. Crystal structure of tetragonal BiFeO_3 shown in a $2 \times 2 \times 2$ supercell. Purple spheres represent Bi ions, brown spheres denote Fe ions located at the centers of corner-sharing FeO_6 octahedra, and red spheres correspond to oxygen ions.

shown in Fig. 1.

All structural and magnetic properties of tetragonal bulk BiFeO_3 are investigated using DFT as implemented in the Vienna *ab initio* Simulation Package (VASP) code [88, 89]. To explore a broad range of magnetic configurations, a $2 \times 2 \times 2$ supercell (see Fig. 2) is chosen for all magnetic calculations [65, 68, 90]. A kinetic energy cutoff of 500 eV is employed for the plane-wave basis set expansion. The Perdew–Burke–Ernzerhof (PBE) version [91] of the generalized gradient approximation (GGA) is adopted as the exchange-correlation functional in conjunction with the projector augmented wave (PAW) method. A $5 \times 5 \times 5$ Monkhorst-Pack k -point grid is used to sample the first Brillouin zone for the self-consistent calculations. When the c/a ratio (the ratio of the out-of-plane to the in-plane lattice parameter) is ≥ 1.1 , the k -point mesh is adjusted to $5 \times 5 \times 4$ to ensure appropriate sampling along the elongated crystallographic direction. To account for the strong on-site Coulomb interactions associated with the localized Fe $3d$ states, we use the GGA+ U approach formulated by Dudarev *et al* [92]. In this scheme, the effective Hubbard parameter $U_{\text{eff}} = U - J$, is set to 4.6 eV for Fe atoms only [65, 68], ensuring a more accurate description of electronic correlations in this transition-metal oxide system.

The crystal structure of BiFeO_3 features a rhombohedral perovskite crystal structure, which is commonly referenced as pseudocubic in this case given its optimized reference lattice parameters ($a = b = c = 3.99 \text{ \AA}$ and $\alpha = \beta = \gamma = 89.34^\circ$) [65]. This structure exhibits a G-type AF phase below 640 K [64]. To systematically analyze the effects of compressive or tensile strain on this model system imposed by a substrate we consider cubic-symmetry-based structures. For each chosen in-plane lattice parameter ($a_s = b_s$), the out-of-plane lattice constant (c_s) is varied independently. The value c_o (optimized c_s parameter), which is the specific c_s that minimizes the total energy of the system, is then calculated. This procedure effectively captures the tetrago-

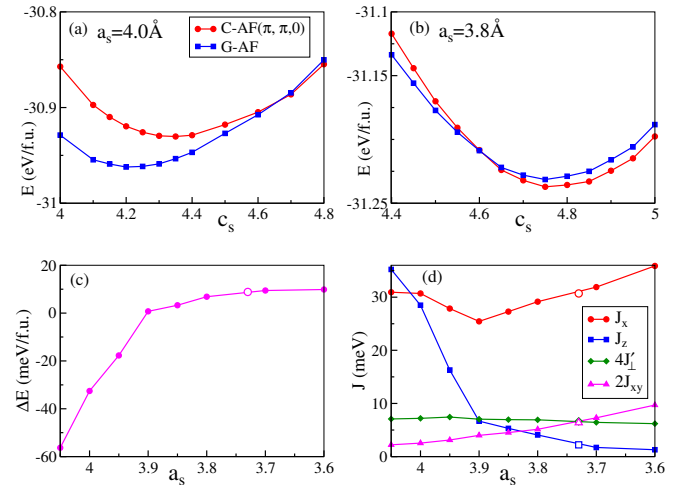


FIG. 3. Energies of G-type AF and C-type AF($\pi, \pi, 0$) phases in BiFeO_3 as a function of the out-of-plane lattice constant c_s , for two fixed in-plane lattice constants: (a) $a_s = 4.0 \text{ \AA}$ and (b) $a_s = 3.8 \text{ \AA}$. As a_s decreases from 4.0 \AA to 3.8 \AA , the magnetic ground state switches from G-type AF to C-type AF($\pi, \pi, 0$). (c) Energy difference $\Delta E = E_G - E_C$ as a function of the in-plane lattice constant a_s , where the out-of-plane lattice parameter c_o is fixed at its optimized value, which minimizes the total energy. As a_s decreases (increasing compressive strain), ΔE gradually increases and eventually becomes positive, indicating a transition from the G-type AF state to the C-type AF($\pi, \pi, 0$) state. (d) Exchange couplings extracted from Table I as a function of the in-plane lattice parameter a_s . For clarity, J'_\perp and J'_{xy} are scaled by a factor of 4 and 2, respectively, highlighting the point near $a_s \approx 3.9 \text{ \AA}$, where $E_G = E_C$. Results corresponding to the volume-relaxed tetragonal structure ($a_s = 3.73 \text{ \AA}$ and $c_o = 4.88 \text{ \AA}$) are also shown in panels (c) and (d) using open symbols. The G-type AF and C-type AF phases are labeled G-AF and C-AF, respectively in all figures.

nal distortion induced by epitaxial strain. For instance, in Fig. 3(a), we fixed the in-plane lattice parameter $a_s = 4.0 \text{ \AA}$ and varied c_s to find the minimum energy. Comparing the energies of the G-type AF, C-type AF, A-type AF, and FM phases, the G-type AF and C-type AF($\pi, \pi, 0$) structures are consistently found to be lower in energy, indicating that the main competition is between these two magnetic states. The total energies per Fe atom of these configurations show the lowest energy achieved by the system occurs near optimal $c_o \approx 4.2 \text{ \AA}$, where the G-type AF state is the ground state. In contrast, for a smaller in-plane lattice constant ($a_s = 3.8 \text{ \AA}$), as shown in Fig. 3(b), the magnetic ground state shifts to the C-type AF($\pi, \pi, 0$) phase for an optimal $c_o = 4.75 \text{ \AA}$. Please note that the equilibrium ground state for the tetragonal structure, as established by the volume relaxation calculation, is characterized by lattice constants $a_s = 3.73 \text{ \AA}$ and $c_o = 4.88 \text{ \AA}$ and exhibits a stable C-type AF magnetic ordering.

Next, we evaluated the energy difference $\Delta E = E_G - E_C$ between G-type AF and C-type AF($\pi, \pi, 0$) configu-

rations, systematically varying the in-plane lattice constant while optimizing the out-of-plane constant. Our results show a clear strain-dependent trend: as the in-plane lattice constant is reduced (compressive strain) from $a_s = 4.0$ Å, $|\Delta E|$ steadily decreases and beyond a critical compression, it changes sign from negative to positive. This confirms that compressive in-plane strain enhances the tendency toward C-type AF($\pi, \pi, 0$) order. We also observed that $|\Delta E|$ increases when a_s is slightly increased toward $a_s \approx 4.05$ Å (tensile strain) from $a_s \approx 4.0$ Å.

Now, to quantitatively describe the microscopic magnetic interactions, we employ the following Heisenberg spin Hamiltonian:

$$H = E_0 + J \sum_{\langle i,j \rangle} \mathbf{s}_i \cdot \mathbf{s}_j + J' \sum_{\langle\langle i,j \rangle\rangle} \mathbf{s}_i \cdot \mathbf{s}_j, \quad (1)$$

where J and J' represent the NN and NNN exchange interactions, respectively. We assume classical spins and set the magnitude $|\mathbf{s}| = 1$, thus absorbing the magnitude of the moment in the exchange parameters. To capture the strain-induced anisotropy, we distinguish between nonequivalent crystallographic directions: the in-plane NN exchange is $J_x = J_y$, the out-of-plane NN exchange is J_z , the NNN exchange along the xz/yz planes is J'_\perp , and the in-plane NNN exchange is J'_{xy} . The total energies of different spin configurations calculated using DFT are mapped onto this model as follows (energies are given per Fe atoms):

$$\begin{aligned} E_G &= E_0 - 2J_x - J_z + 4J'_\perp + 2J'_{xy}, \\ E_C &= E_0 - 2J_x + J_z - 4J'_\perp + 2J'_{xy}, \\ E_A &= E_0 + 2J_x - J_z - 4J'_\perp + 2J'_{xy}, \\ E_F &= E_0 + 2J_x + J_z + 4J'_\perp + 2J'_{xy}, \\ E_{A'} &= E_0 + J_z - 2J'_{xy}, \end{aligned}$$

to determine five parameters E_0 , J_x , J_z , J'_\perp , J'_{xy} . Here E_G , E_C , E_A , $E_{A'}$, and E_F correspond to the G-type AF, C-type AF($\pi, \pi, 0$), A-type AF($0, 0, \pi$), A-type AF($0, \pi, 0$), and FM states, respectively (see Fig. 1 for schematic illustrations of the magnetic phases). The extracted exchange couplings, listed in Table I, reveal clear anisotropic trends induced by epitaxial strain. Specifically, as the in-plane lattice constant a_s decreases (and c_o increases), the out-of-plane coupling J_z decreases substantially. Concurrently, the in-plane NNN coupling J'_{xy} increases as a_s decreases, while the out-of-plane NNN coupling J'_\perp varies only weakly with strain. These significant anisotropies are crucial in determining which of the competing AF states is the magnetic ground state.

A more quantitative picture of the strain effects emerges from Fig. 3(d), in which we plot the exchange couplings extracted via the DFT mapping (from Table I). For clarity in analyzing the dominant interactions, the out-of-plane NNN exchange J'_\perp is scaled by a factor of four to highlight the crossover between $4 \times J'_\perp$ and J_z near

TABLE I. Direction-dependent exchange couplings ($J_x = J_y$, J_z , J'_\perp , and J'_{xy}) in BiFeO₃ obtained from DFT calculations at different in-plane lattice constants a_s . The corresponding out-of-plane lattice constant c_o is the optimized value for that particular a_s (e.g., $c_o = 4.2$ Å when $a_s = 4.0$ Å). Exchange couplings for $a_s = 3.73$ Å and $c_o = 4.88$ Å (volume-relaxed tetragonal structure) are also provided. All J values are given in meV.

a_s (Å)	c_o (Å)	$J_x = J_y$	J_z	J'_\perp	J'_{xy}
4.05	4.10	30.93	35.22	1.77	1.11
4.00	4.20	30.70	28.48	1.80	1.27
3.95	4.40	27.86	16.29	1.86	1.56
3.90	4.65	25.44	6.67	1.76	2.00
3.85	4.70	27.28	5.31	1.74	2.26
3.80	4.75	29.15	4.07	1.73	2.57
3.73	4.88	30.70	2.21	1.66	3.19
3.70	4.95	31.89	1.72	1.61	3.65
3.60	5.00	35.87	1.29	1.55	4.85

$a_s \approx 3.9$ Å, which is precisely where the energies of the G-type AF and C-type AF($\pi, \pi, 0$) states nearly balance, as shown in Fig. 3(b). This reflects the direct competition between these two exchange mechanisms given the in-plane AF configuration: A large J_z promotes the G-type AF order by stabilizing AF alignment between out-of-plane NN Fe ions, while a larger $4 \times J'_\perp$ tends to stabilize the C-type AF($\pi, \pi, 0$) phase as it favors AF coupling between NNN Fe ions along the out-of-plane direction. The factor of four arises because each Fe ion has eight out-of-plane NNNs but only two NNs along the z -direction, meaning the NNN contribution is weighted by a factor of four when comparing to the NN contribution to the total energy difference between G-type AF and C-type AF states. When $4J'_\perp > J_z$, the NNN contribution becomes dominant, and the C-type AF($\pi, \pi, 0$) order overtakes the G-type AF state as the preferred magnetic configuration. Thus, the crossover explicitly reflects the competition between the weakening of the NN out-of-plane AF exchange (J_z) and the strengthening of the NNN out-of-plane exchange (J'_\perp) under strain. Finally, please note that the in-plane couplings satisfy $2J'_{xy} < J_x$ throughout the studied strain range, indicating the persistent dominance of the in-plane NN AF interaction.

The next step in parameterizing our Hubbard model, discussed in the next section, is to translate the DFT-derived exchange couplings into hopping amplitudes using the superexchange relationship $J \approx t^2/U$ where U is the on-site repulsive Hubbard interaction strength. The hopping parameter t_x is calculated to be 0.37 eV given an exchange coupling J_x of 30 meV and an on-site repulsive Hubbard interaction strength (U) of 4.6 eV. Notably, the ratio of U to t_x is approximately 12.43, which is a trademark of a strongly correlated electron system. With in-plane hopping t_x set to unity as the reference scale, the normalized parameters are listed in Table II. Please note, for $a_s = 4.0$ Å, t_z nearly equals t_x ($t_z/t_x \approx 0.963$), in-

TABLE II. Normalized hopping amplitudes $t_x = t_y$, t_z , t'_{\perp} and t'_{xy} for BiFeO₃ are derived from the exchange couplings $J_x = J_y$, J_z , J'_{\perp} and J'_{xy} , respectively presented in Table I. These hopping amplitudes are calculated using the relation $t/t_x \approx \sqrt{J/J_x}$, based on the approximation $J \propto t^2/U$, where U represents the on-site Hubbard interaction (t_x is set to 1).

a_s (Å)	c_o (Å)	$t_x = t_y$	t_z	t'_{\perp}	t'_{xy}
4.05	4.10	1.00	1.067	0.239	0.189
4.00	4.20	1.00	0.963	0.242	0.203
3.95	4.40	1.00	0.765	0.258	0.237
3.90	4.65	1.00	0.512	0.263	0.280
3.85	4.70	1.00	0.441	0.253	0.288
3.80	4.75	1.00	0.374	0.244	0.297
3.73	4.88	1.00	0.268	0.233	0.322
3.70	4.95	1.00	0.232	0.225	0.338
3.60	5.00	1.00	0.190	0.208	0.368

dicating an almost isotropic three-dimensional hopping regime. As expected, the out-of-plane hopping t_z decreases considerably as the in-plane lattice constant is reduced (i.e., under compressive strain), transitioning the system from a nearly isotropic 3D regime to a highly anisotropic regime and selectively tuning the ratio of out-of-plane to in-plane hopping amplitudes. Elaborately, for the smaller in-plane lattice constant, for example $a_s = 3.6$ Å, t_z drops to approximately 0.19, showing that the out-of-plane hopping amplitude is much weaker than the in-plane hopping amplitudes. Furthermore, the NNN hoppings, t'_{\perp} and t'_{xy} , change only moderately with strain. Notably, the value of $2 \times t'_{\perp}$ roughly matches t_z for $a_s = 3.9$ Å, which is precisely the lattice constant where the G-type and C-type AF phases compete as the ground state. This direct correspondence is a clear result of our earlier analysis, as expected, where the related exchange couplings $4 \times J'_{\perp}$ and J_z were found to be comparable at the same parameter value. Overall, these results demonstrate that epitaxial strain selectively tunes the ratio t_z/t_x . Thus, our first-principles results provide direct physical intuition for our model analysis: epitaxial strain does not simply change the overall bandwidth, but selectively modifies the ratio of out-of-plane to in-plane hopping amplitudes. This induced anisotropy, which drives the magnetic transition, provides the key motivation for our systematic study of the anisotropic Hubbard model at large on-site repulsive Hubbard interaction strength.

III. MODEL HAMILTONIAN AND COMPUTATIONAL METHOD

In order to investigate the strain-driven magnetotransport properties, we consider the following form of the one-band half-filled Hubbard Hamiltonian on a simple cubic

lattice with periodic boundary conditions [78, 81, 93, 94]:

$$H = -t \sum_{\langle i,j \rangle, \sigma} c_{i,\sigma}^\dagger c_{j,\sigma} - t' \sum_{\langle\langle i,j \rangle\rangle, \sigma} c_{i,\sigma}^\dagger c_{j,\sigma} + U \sum_i n_{i,\uparrow} n_{i,\downarrow} - \mu \sum_i n_i = H_0 + H_I, \quad (2)$$

Here, t and t' represent the NN and NNN hopping amplitudes, respectively. $c_{i,\sigma}^\dagger$ ($c_{i,\sigma}$) creates (annihilates) an electron at site i with spin σ and n_i ($= \sum_{\sigma} c_{i,\sigma}^\dagger c_{i,\sigma}$) is the total number operator at site i . Furthermore, U (> 0) is the on-site repulsive Hubbard interaction strength, and μ is the chemical potential controlling the overall carrier density of the system. Finally, the Hamiltonian is formally split into a non-interacting quadratic part H_0 and an interaction quartic term H_I .

To make the model tractable, we decouple the H_I part using the Hubbard-Stratonovich (HS) transformation, which introduces auxiliary fields \mathbf{m}_i and ϕ_i at each site. The vector field \mathbf{m}_i and the scalar field ϕ_i are associated with spin and charge fluctuations, respectively. Next, we assume that the HS auxiliary fields are static in imaginary time and treat them as classical variables. At the saddle-point approximation, we relate the scalar auxiliary field ϕ_i to the local charge density n_i by imposing $i\phi_i = \frac{U}{2}\langle n_i \rangle$, effectively making ϕ_i proportional to the average charge density ($\langle n_i \rangle$). However, the auxiliary fields remain spatially non-uniform and experience thermal fluctuations, which are crucial for capturing finite-temperature magnetic and electronic phases. It is worth emphasizing that the HS transformation operates locally at each lattice site, enabling the decoupling of the on-site interaction term. Using these approximations (for details, see Appendix A), we obtain the following effective spin-fermion Hamiltonian [81–87]:

$$H_{\text{eff}} = -t \sum_{\langle i,j \rangle, \sigma} c_{i,\sigma}^\dagger c_{j,\sigma} - t' \sum_{\langle\langle i,j \rangle\rangle, \sigma} c_{i,\sigma}^\dagger c_{j,\sigma} + \frac{U}{2} \sum_i (\langle n_i \rangle n_i - \mathbf{m}_i \cdot \boldsymbol{\sigma}_i) + \frac{U}{4} \sum_i (\mathbf{m}_i^2 - \langle n_i \rangle^2) - \mu \sum_i n_i, \quad (3)$$

where $\boldsymbol{\sigma}_i$ is the vector of Pauli matrices.

To solve the effective model, we employ the well studied s-MC method. For any given configuration of auxiliary fields $\{\mathbf{m}_i\}$ and average charge densities $\{\langle n_i \rangle\}$, the effective Hamiltonian is initially diagonalized. The system is then simulated at a fixed temperature, where each lattice site is sequentially updated using the Metropolis algorithm to anneal the auxiliary spin fields $\{\mathbf{m}_i\}$. The system undergoes 2000 Monte Carlo sweeps per temperature step: the first 1000 for thermal equilibration and the remaining 1000 for measuring observables. To ensure the system maintains the half-filled condition ($n = 1$), the charge densities $\{\langle n_i \rangle\}$ and the chemical potential μ are updated self-consistently every 10 MC

sweeps. Physical observables are computed from 100 statistically independent equilibrium configurations, with measurements taken from every 10th configuration to reduce autocorrelation. We further average over 10 independent Monte Carlo calculations starting from different initial auxiliary-field configurations. To ensure thorough equilibration, the temperature is decreased gradually from high temperatures. Furthermore, we implement the traveling-cluster approximation (TCA) [83–87, 95] using a 4^3 update cluster that allows us to perform simulations on large system sizes, specifically $L^3 = 10^3$, which significantly helps to mitigate finite-size effects.

We incorporate direction-dependent hopping terms in the Hubbard model to account for the anisotropy arising from the strain in the materials as discussed in previous section. We subgroup the three NN hopping parameters, t_x , t_y , and t_z , corresponding to hopping along the x , y , and z directions, respectively, into two distinct groups: $t_x = t_y$ and t_z . Additionally, we include NNN hopping parameters, t'_{xy} , t'_{yz} , and t'_{xz} , corresponding to hopping in the xy , yz , and xz planes, and define $t'_\perp = t'_{yz} = t'_{xz}$. To maintain consistency across our s-MC simulations, we set $t_x = t_y = 1$ and express all other hopping parameters relative to t_x . For analyzing the effects of compressive and tensile epitaxial strain, we tune the values of t_z , t'_{xy} , and t'_\perp . We vary $0 \leq t_z \leq 2$, where $t_z < 1$ ($t_z > 1$) represents compressive (tensile) strain in the xy -plane. For the NNN hopping terms, we consider $0 \leq t'_{xy} \leq 1$ and $0 \leq t'_\perp \leq 2$. The basis for selecting this range of hopping parameters was discussed previously using DFT calculations. Furthermore, the on-site repulsive Hubbard interaction strength (U), the bare bandwidth (W), and the temperature (T) are measured relative to the hopping amplitude (t_x). This ensures that the energy scales of the interaction and thermal effects are consistently defined relative to the hopping processes.

To gain deeper insight into the magnetotransport properties of the system, we evaluate a range of physical observables. The magnetic behavior is characterized by calculating the local magnetic moments M and the spin structure factor $S(\mathbf{q})$, which captures quantum spin correlations. Representative magnetic spin configurations on a simple cubic lattice, characterized by distinct ordering vectors \mathbf{q} , are shown in Fig. 1. We also examine the temperature dependence of the specific heat C_v , looking for low-temperature peaks that signals the magnetic ordering phenomena. Transport characteristics are analyzed through the resistivity along the z direction ρ_z , defined as the inverse of the dc limit of the optical conductivity, along with the electronic density of states (DOS). A detailed description of these observables and their computational implementation is provided in Appendix B.

We set the on-site repulsive Hubbard interaction strength U to be equal to W (≈ 12), the bare bandwidth. This choice of U value is consistent with the DFT calculation in the previous section, where the ratio of U and t_x was found to be 12.43. To further justify this parameter choice, we calculate the Néel tem-

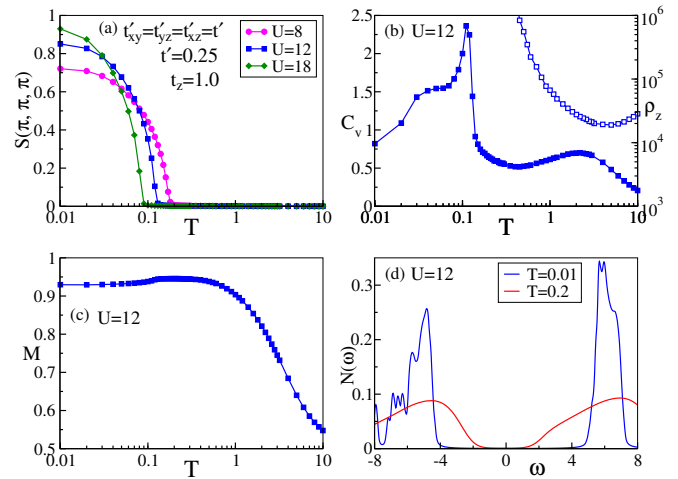


FIG. 4. (a) Temperature dependent of $S(\pi, \pi, \pi)$ for isotropic NN ($t_x = t_y = t_z = 1$) and NNN hoppings ($t'_{xy} = t'_{yz} = t'_{xz} = 0.25$). The system undergoes a G-type AF transition with $T_N \approx 0.18$, 0.13 , and 0.09 for $U = 8$, 12 , and 18 , respectively (see main text for details). (b) Temperature dependence of the specific heat C_v (left axis, solid symbols) and resistivity along the z direction ρ_z (right axis, open symbols) for $U = 12$. The low- T peak in C_v marks the onset of long-range magnetic order, while the broad high- T peak signals local-moment formation and coincides with the metal-insulator transition temperature T_{MIT} . (c) Temperature evolution of the local magnetic moment M for $U = 12$; the magnitude of M grows continuously upon cooling and saturates, reflecting the formation of localized magnetic moments at low temperatures. (d) DOS at $T = 0.01$ and $T = 0.2$, both showing a clear gap at the Fermi level ($\omega = 0$). While the gap is wider at $T = 0.01$, it remains distinctly visible even at $T = 0.2 > T_N$, confirming the robustness of the insulating state well above the magnetic ordering temperature. In all calculations, the DOS is shifted such that $\omega = 0$ corresponds to the Fermi level (chemical potential).

perature T_N from the temperature dependence of the magnetic structure factor $S(\pi, \pi, \pi)$, shown in Fig. 4(a) and compare with experimental results. For isotropic NN hopping ($t_x = t_y = t_z = 1$) and isotropic NNN hopping ($t'_{xy} = t'_{yz} = t'_{xz} = 0.25$) the system undergoes a G-type AF transition at $T_N \approx 0.13$ for $U = 12$. These parameters are consistent with the exchange constants extracted for $a_s = 4.0$ and $c_o = 4.2$ in the DFT calculations (see Table II). Using the DFT-derived hopping amplitude $t_x \approx 0.37$ eV, this corresponds to a Néel temperature of approximately 560 K, which reasonably matches the experimental value reported for bulk BiFeO₃ ($T_N \approx 640$ K). For comparison, $U = 8$ and $U = 18$ [also plotted in Fig. 4(a)] provide estimates of $T_N \approx 770$ K and $T_N \approx 390$ K, respectively, both significantly deviating from the experimentally measured value. Consequently, we set $U = 12$ for the remainder of this work.

For completeness, we plot various other physical observables using $U = 12$ with $t_x = t_y = t_z = 1$ and $t'_{xy} = t'_{yz} = t'_{xz} = 0.25$. The specific heat C_v ,

shown in Fig. 4(b), exhibits two distinct features: a sharp low-temperature peak that coincides with the magnetic transition at T_N , and a broad high-temperature peak that signals the formation of local magnetic moments [96]. The separation of these two peaks highlights that moment formation and long-range magnetic ordering occur on different temperature scales, a characteristic feature of strongly correlated electronic systems. The high-temperature peak coincides with the metal-insulator transition temperature (T_{MIT}) extracted from the resistivity ρ_z [also plotted in Fig. 4(b)], indicating that the establishment of local moments is closely tied to the opening of an electronic gap. The temperature dependence of the local magnetic moment, M , shown in Fig. 4(c), further confirms that moment formation happens well above the onset of long-range AF order and eventually saturates at low temperatures. The DOS obtained at $T = 0.01$ in Fig. 4(d) reveals a clear gap at the Fermi level ($\omega = 0$), confirming the insulating nature of the ordered ground state. The gap remains clearly visible even at $T = 0.2$, which is larger than T_N . The emergence of a gap at low temperature, in combination with the thermodynamic and transport signatures at intermediate and large temperatures, establishes that the Mott insulating character of the system persists across the AF transition. This confirms $T_{\text{MIT}} \gg T_N$ and ensures a wide PM insulating (PM-I) regime at intermediate temperatures.

IV. EFFECT OF ANISOTROPIC HOPPING: MODELLING THE COMPRESSIVE STRAIN

The comprehensive DFT calculations, summarized by the derived hopping amplitudes in Table II, reveal the critical role of hopping anisotropy—the key mechanism through which epitaxial strain alters magnetic ordering in perovskite oxides such as BiFeO_3 . Strain primarily modifies the relative strengths of the in-plane (t_x, t_y) and out-of-plane (t_z) hoppings, thereby directly influencing the competition between different AF correlations. To uncover the microscopic evolution of magnetotransport properties under this anisotropic hopping, we examine finite-temperature observables for $U = 12$ while fixing the out-of-plane NN hopping to $t_z = 0.5$ (mimicking the compressive strain) and varying the isotropic NNN hopping t' . The magnetic structure factors shown in Fig. 5(a) clearly distinguish the competing magnetic states. For small t' ($= 0.0$ and 0.2), $S(\pi, \pi, \pi)$ exhibits a well-defined transition into a G-type AF state, with the corresponding Néel temperature T_N decreasing slightly as t' increases. This decrease reflects enhanced magnetic frustration introduced by NNN hopping, which weakens the three-dimensional AF correlations. For larger t' ($= 0.4$), the magnetic correlations shift to $S(\pi, \pi, 0)$, signaling a crossover from G-type AF to C-type AF($\pi, \pi, 0$) order.

The specific heat C_v curves, shown in Fig. 5(b), dis-

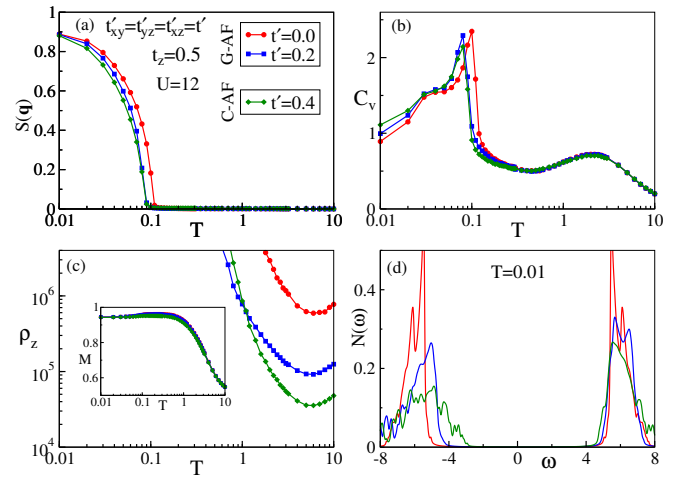


FIG. 5. Magnetic and transport properties for $t_z = 0.5$, with varying isotropic NNN hopping $t' = 0.0, 0.2$, and 0.4 ($t' = t'_{xy} = t'_{yz} = t'_{xz} = t'$): (a) Magnetic structure factor $S(\mathbf{q})$ indicating G-type AF(π, π, π) ordering for $t' = 0$ and 0.2 , and C-type AF($\pi, \pi, 0$) order at $t' = 0.4$. (b) Specific heat C_v displaying low- T peaks that align with the magnetic transitions in (a), and high- T peaks related to moment formation near T_{MIT} . (c) Resistivity ρ_z showing insulating behavior for all t' . Notably, $T_{\text{MIT}} \gg T_N$, leading to a PM-I regime between the paramagnetic metal (PM-M) and magnetically ordered phases. Inset: Temperature dependence of the local magnetic moment M , which saturates at low T , reflecting moment formation well above T_N . (d) DOS at $T = 0.01$ confirming insulating ground states with a finite gap at $\omega = 0$. Legends are consistent across all panels.

play sharp low-temperature peaks, which track the magnetic transitions identified in Fig. 5(a). These peaks, related to spin fluctuations, thermodynamically verify the ordering temperatures. A broad high-temperature peak, originating from charge fluctuations, persists across all t' , indicating the robust formation of local magnetic moments [96]. The temperature dependence of the local magnetic moment, M , shown in the inset of Fig. 5(c), further confirms that moments are well formed at low temperatures for all three t' values. The main panel of Fig. 5(c) shows that the resistivity along the z direction, ρ_z , remains insulating at low temperatures for all t' values, although T_{MIT} decreases slightly with increasing t' . This observed insulating behavior is consistently supported by the low-temperature DOS in Fig. 5(d), which reveals a gap around the Fermi level ($\omega = 0$). Furthermore, we note that T_{MIT} matches well with the temperature at which the high-temperature peak in C_v appears [as discussed for the isotropic hopping case, in Fig. 4(b)]. Importantly, T_{MIT} always exceeds T_N , which ensures the existence of a substantial PM-I regime between the PM-M and AF insulating states.

We now map out the $t'-T_N$ phase diagram for isotropic NNN hopping ($t'_{xy} = t'_{yz} = t'_{xz} = t'$) in Fig. 6(a). As the temperature is lowered, the system evolves from the high-temperature PM-I regime, transitioning into a G-

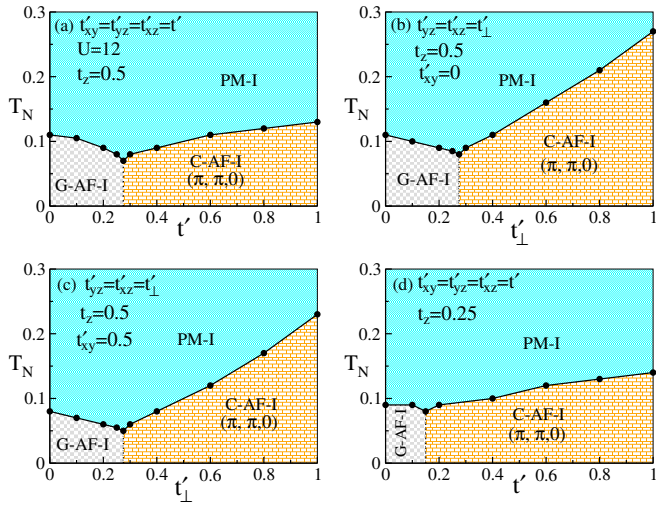


FIG. 6. (a) The t' - T_N phase diagram for isotropic NNN hopping ($t'_{xy} = t'_{yz} = t'_{xz} = t'$) at $t_z = 0.5$. Small t' favors a G-type AF insulating phase, while moderate-to-large t' stabilizes a C-type AF($\pi, \pi, 0$) insulating phase. As t' increases, T_N decreases within the G-type AF regime but increases for the C-type AF phase. The t'_\perp - T_N phase diagrams ($t'_{yz} = t'_{xz} = t'_\perp$) with $t_z = 0.5$ for two in-plane NNN hoppings: (b) $t'_{xy} = 0$ and (c) $t'_{xy} = 0.5$. In both cases, increasing t'_\perp drives a transition from G-type AF at small t'_\perp to C-type AF at larger values. The transition point is essentially identical to that in (a), suggesting the in-plane NNN hopping does not shift the crossover boundary, though T_N is suppressed for $t'_{xy} = 0.5$. (d) The t' - T_N phase diagram for isotropic NNN hopping at a smaller out-of-plane hopping $t_z = 0.25$. Reducing t_z shifts the G-type AF to C-type AF crossover to lower t' values. In all cases, $T_{\text{MIT}} \gg T_N$, giving rise to a PM-I regime above the T_N . The G-type and C-type AF phases are labeled as G-AF-I and C-AF-I, respectively; notably, all magnetic phases reported in this work are insulating.

type AF insulator for small t' but stabilizing a C-type AF($\pi, \pi, 0$) insulating state for moderate to large t' . Increasing t' monotonically suppresses the G-type AF ordering temperature (T_N) due to the enhanced magnetic frustration introduced by the NNN hopping. This G-type AF order persists until a critical value of $t' \approx 0.27$, beyond which the system stabilizes the C-type AF($\pi, \pi, 0$) phase, and T_N subsequently increases with further increments in t' . Crucially, the anisotropy in the NN hopping ($t_x = t_y \neq t_z$) explicitly lifts the degeneracy of the C-type AF orders [i.e., between the $(\pi, \pi, 0)$, $(0, \pi, \pi)$, and $(\pi, 0, \pi)$ variants] that arises from cubic symmetry. Since $t_z < t_x$, the out-of-plane AF order is weaker than the in-plane AF order; consequently, only the C-type AF($\pi, \pi, 0$) configuration is stabilized in the phase diagram for large t' , while the symmetry-related $(0, \pi, \pi)$ and $(\pi, 0, \pi)$ variants are suppressed. Throughout this evolution, T_{MIT} remains higher than T_N , which maintains a broad PM-I intermediate regime, consistent with the magnetic and transport behavior reported in Fig. 5.

At this point it is important to mention that while the

isotropic t' analysis identifies the dominant role of NNN hopping in controlling the magnetic phase competition, realistic epitaxial strain environments are expected to modify the in-plane and out-of-plane NNN hopping amplitudes differently. This raises a critical question: which NNN hopping component—the out-of-plane component ($t'_\perp = t'_{yz} = t'_{xz}$) or the in-plane component (t'_{xy})—plays the major role in driving the magnetic phase transition? To address this, we analyze the t'_\perp - T_N phase diagrams for anisotropic NNN hopping configurations shown in Figs. 6(b) and 6(c). In these plots, the out-of-plane component t'_\perp is varied at a fixed $t_z = 0.5$ (compressive strain) for two representative in-plane values: $t'_{xy} = 0$ [Fig. 6(b)] and $t'_{xy} = 0.5$ [Fig. 6(c)]. In both cases, increasing t'_\perp drives a transition from a G-type AF state to a C-type AF($\pi, \pi, 0$) phase. Remarkably, the transition point for the G-type AF to C-type AF($\pi, \pi, 0$) crossover is essentially identical to that found in the isotropic NNN hopping case [Fig. 6(a)]. This strongly suggests that the crossover boundary is governed primarily by the out-of-plane NNN hopping t'_\perp rather than the in-plane component t'_{xy} , a result that is physically viable in real systems given that the required t'_\perp is around $t_z/2$ to drive this transition.

However, t'_{xy} does influence the ordering temperature: when the in-plane competition is absent ($t'_{xy} = 0$), the T_N corresponding to the C-type AF($\pi, \pi, 0$) phase grows rapidly with increasing t'_\perp . Conversely, when a finite in-plane NNN hopping is included ($t'_{xy} = 0.5$), the overall Néel temperature decreases across all t'_\perp . This confirms that the in-plane NNN hopping t'_{xy} mainly modulates the ordering temperature under compressive strain ($t_z = 0.5$).

Next, we investigate the isotropic NNN hopping case by setting the out-of-plane NN hopping to $t_z = 0.25$ to focus on the effects of stronger compressive strain. This allows us to quantify how strain shifts the balance between competing AF orders. The resulting t' - T_N phase diagram is displayed in Fig. 6(d). Under these conditions, the transition from G-type AF to C-type AF($\pi, \pi, 0$) occurs at a smaller critical t' (≈ 0.15), confirming that compressive strain enhances the tendency toward C-type AF($\pi, \pi, 0$) order at much smaller t' . Similar to the behavior observed at $t_z = 0.5$, in this more extreme compressive regime ($t_z = 0.25$), the primary role of the in-plane NNN hopping, t'_{xy} , is to modulate the magnetic ordering temperature. However, crucially, t'_{xy} does not significantly control the magnetic phase transition point at low temperatures, which is predominantly controlled by the out-of-plane NNN hopping, t'_\perp .

The finite-temperature analysis above demonstrates that the competition between G-type AF and C-type AF($\pi, \pi, 0$) orders is strongly controlled by the strengths of both out-of-plane NN and NNN hopping amplitudes. To present the complete picture of how the ground state phases behave with t_z and t' , we show the t_z - t' phase diagram at a low temperature ($T = 0.01$) in Fig. 7(a). Note that, in this section, our analysis focuses only on

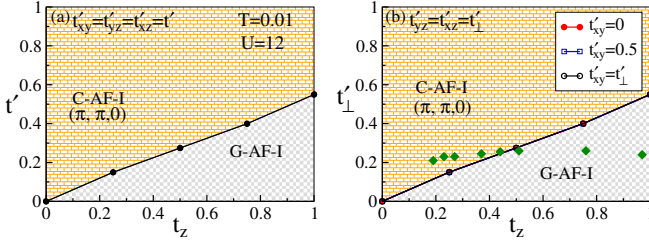


FIG. 7. (a) Low-temperature ($T = 0.01$) t_z - t' phase diagram for isotropic NNN hoppings. Increasing t' drives a transition from the G-type AF insulating state to a C-type AF insulating state. The critical t' value increases linearly as t_z increases. (b) The t_z - t'_\perp phase diagrams ($t'_{yz} = t'_{xz} = t'_\perp$) shown for $t'_{xy} = 0$ and $t'_{xy} = 0.5$; the isotropic NNN hopping case ($t'_{xy} = t'_\perp$) is replotted for comparison. In all cases, increasing t'_\perp destabilizes the G-type AF phase in favor of C-type AF order, while the phase boundary remains independent of t'_{xy} . Green diamonds mark the parameter sets obtained from DFT (see Table II).

the $t_z < t_x$ regime, which corresponds to compressive strain. As the isotropic NNN hopping t' increases, the system evolves from a G-type AF insulator to a C-type AF($\pi, \pi, 0$) insulator in the whole range. The critical t' separating these phases grows monotonically with increasing t_z , as a larger out-of-plane NN hopping t_z stabilizes AF alignment along the z -axis and delays the ferromagnetic stacking required for the C-type AF($\pi, \pi, 0$) state.

Next, focusing on the relative roles of in-plane and out-of-plane NNN hopping, we show the t_z - t'_\perp phase diagram at $T = 0.01$ with varying t'_{xy} in Fig. 7(b). In all cases shown ($t'_{xy} = 0$, $t'_{xy} = 0.5$, and $t'_{xy} = t'_\perp$), increasing the out-of-plane NNN hopping t'_\perp destabilizes the G-type AF phase and stabilizes the C-type AF($\pi, \pi, 0$) order. Notably, the phase boundary between the G-type AF and C-type AF($\pi, \pi, 0$) order remains nearly unchanged across all three t'_{xy} values. This highlights that for $t_z < t_x$ (under compressive strain), the out-of-plane NNN hopping t'_\perp is the main driver of the G-type AF to C-type AF($\pi, \pi, 0$) transition, while variations in in-plane NNN hopping t'_{xy} primarily influence the ordering temperature (as seen in Fig. 6).

The magnetic phase boundary in Fig. 7(b), marking the transition from G-type to C-type AF($\pi, \pi, 0$), is consistently found near the hopping ratio $t'_\perp/t_z \approx 0.5$. This result is fully consistent with the DFT-derived crossing point, which shows the magnetic crossover is governed by $J'_\perp/J_z \approx 0.25$ (Fig. 3), based on the underlying superexchange mechanism $J \sim t^2/U$. These $J'_\perp/J_z \approx 0.25$ or $t'_\perp/t_z \approx 0.5$ conditions signify the point where the out-of-plane NN AF interaction is balanced by the frustrating out-of-plane NNN AF interaction. The location of the DFT-derived hopping parameters (indicated by diamond symbols in Fig. 7(b) and listed in Table II) near the G-type AF to C-type AF($\pi, \pi, 0$) boundary confirms that a small change in out-of-plane NN hopping can

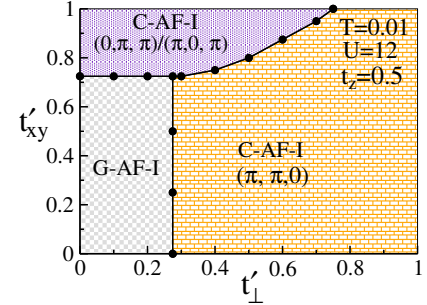


FIG. 8. The t'_\perp - t'_{xy} phase diagram at $T = 0.01$ for $t_z = 0.5$ (representing compressive strain). At small t'_{xy} , increasing t'_\perp drives a transition from the G-type AF insulating state to the C-type AF($\pi, \pi, 0$) insulating phase. Conversely, for large in-plane NNN hopping ($t'_{xy} \gtrsim 0.72$), a twofold-degenerate C-type AF[$(0, \pi, \pi)/(\pi, 0, \pi)$] phase is stabilized at small t'_\perp . Within this large- t'_{xy} regime, increasing t'_\perp induces a switching between the C-type AF[$(0, \pi, \pi)/(\pi, 0, \pi)$] and C-type AF($\pi, \pi, 0$) phases.

switch the magnetic ground state. Overall, these results demonstrate that the anisotropic hopping framework is minimal yet effective for capturing and predicting the strain-induced magnetic ground state switch.

Finally, to present the full magnetic phase behavior across the parameter space, we show the t'_\perp - t'_{xy} phase diagram in Fig. 8 for $t_z = 0.5$. Here, we varied t'_{xy} up to a value of 1 for completeness, though we acknowledge that such a large magnitude relative to t_x is highly improbable in realistic material systems. Beyond a critical, high value of t'_{xy} (approximately ~ 0.72), the twofold-degenerate C-type AF[$(0, \pi, \pi)/(\pi, 0, \pi)$] phase appears as the ground state, particularly for small values of the out-of-plane NNN hopping, t'_\perp . Furthermore, in this high t'_{xy} regime (e.g., around $t'_{xy} \sim 0.8$), increasing t'_\perp triggers a subtle intra-C-type phase transition, causing a switching of the ground state between the C-type variants: AF[$(0, \pi, \pi)/(\pi, 0, \pi)$] and AF($\pi, \pi, 0$) phase.

V. EFFECT OF ANISOTROPIC HOPPING: MODELLING THE TENSILE STRAIN

Our calculations in the previous section established that compressive epitaxial strain ($t_z < t_x$) strongly enhances the competition between two types of magnetic order, namely G-type and C-type AF order, with NNN hopping selectively stabilizing the C-type AF($\pi, \pi, 0$) state; however, the magnetic competition is expected to be qualitatively modified under tensile strain ($t_z > t_x$), where the out-of-plane NN hopping becomes the dominant coupling. To determine how this balance evolves, we now examine the finite-temperature phase diagram for a representative large value, $t_z = 2.0$, and analyze its interplay with both isotropic and anisotropic NNN hopping. For isotropic NNN hopping, $t'_{xy} = t'_{yz} = t'_{xz} = t'$ [see Fig. 9(a)], the system shifts from a high-temperature

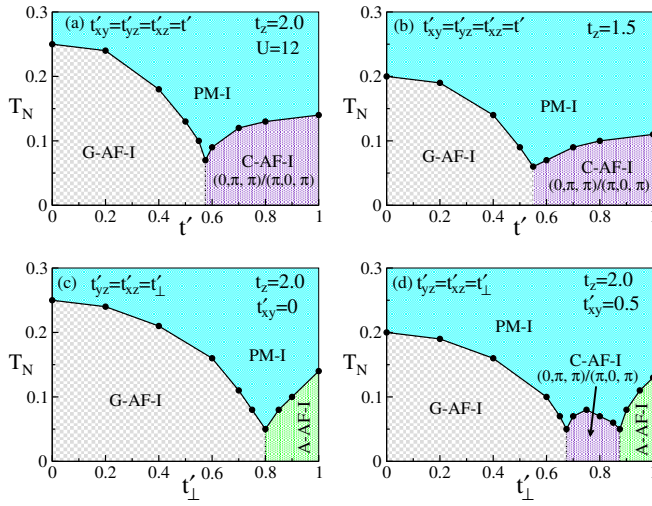


FIG. 9. Finite-temperature phase diagrams for isotropic and anisotropic NNN hoppings under tensile strain ($t_z > t_x$). (a, b) The t' - T_N phase diagrams for isotropic NNN hoppings ($t'_{xy} = t'_{yz} = t'_{xz} = t'$) at (a) $t_z = 2.0$ and (b) $t_z = 1.5$. For both t_z values, the system orders into a G-type AF insulating state at small t' , whereas larger t' stabilizes a twofold-degenerate C-type AF $[(0, \pi, \pi)/(\pi, 0, \pi)]$ insulating phase. Across the G-type AF region, T_N decreases monotonically with increasing t' , while in the C-type AF region, T_N increases with t' . Reducing t_z from 2.0 to 1.5 suppresses T_N overall, though the qualitative features of the phase diagram remain unchanged. (c, d) The t'_\perp - T_N phase diagrams for anisotropic NNN hopping ($t'_{yz} = t'_{xz} = t'_\perp$) at $t_z = 2.0$ with (c) $t'_{xy} = 0$ and (d) $t'_{xy} = 0.5$. In the absence of in-plane NNN hopping, the twofold-degenerate C-type AF $[(0, \pi, \pi)/(\pi, 0, \pi)]$ phase is fully suppressed; instead, an A-type AF $(0, 0, \pi)$ insulating phase emerges at large t'_\perp , and the G-type AF region expands relative to (a). With finite in-plane hopping ($t'_{xy} = 0.5$), the phase diagram becomes richer: the G-type AF insulating phase persists up to intermediate t'_\perp , followed by a narrow window of the twofold-degenerate C-type AF $[(0, \pi, \pi)/(\pi, 0, \pi)]$ phase, and finally an A-type AF $(0, 0, \pi)$ state at large t'_\perp . Interestingly, for $t'_{xy} = 0.5$, T_N exhibits a non-monotonic trend within the twofold-degenerate C-type AF $[(0, \pi, \pi)/(\pi, 0, \pi)]$ region, while it continues to decrease monotonically for G-type AF and increase for A-type AF $(0, 0, \pi)$ orders. In all panels, T_{MIT} remains significantly higher than T_N , resulting in a finite-temperature PM-I regime. A-type AF $(0, 0, \pi)$ insulating phase is labeled as A-AF-I in all figures.

PM-I phase into a G-type AF insulator at small t' , but the ground state switches to a twofold-degenerate C-type AF phase, corresponding to ordering vectors $(0, \pi, \pi)$ and $(\pi, 0, \pi)$, at large t' .

The analysis of the tensile strain regime ($t_z > t_x$) reveals three primary consequences arising from the dominant out-of-plane NN hopping. The first key finding is the overall enhancement of the T_N of the G-type AF phase, directly attributable to the large t_z which drives the AF order to higher temperatures. The second key finding is the complete absence of the C-type AF $(\pi, \pi, 0)$

phase [which was present in the small- t_z regime (see Fig. 6)] when t_z is large. This difference also stems from the large out-of-plane NN hopping: since $t_z > t_x$, the NN AF coupling along the z direction becomes dominant over in-plane NN AF interactions. Consequently, the system naturally favors magnetic orders that preserve out-of-plane antiferromagnetism, leading to the stabilization of the twofold-degenerate C-type AF $[(0, \pi, \pi)/(\pi, 0, \pi)]$ phase at large t' . The third key finding is that the G-type AF order persists up to significantly larger NNN hopping (t') values compared to the small- t_z case [see Fig. 6(a)]. The G-type AF phase maintains its stability over an extended intermediate range of t' due to two combined effects: the increasing influence of the NN hopping parameters with larger t_z , and the degeneracy of the competing C-type AF phase between the $(0, \pi, \pi)$ and $(\pi, 0, \pi)$ ordering vectors. Consistent with the small- t_z regime, the T_N decreases monotonically with t' in the G-type AF phase, while it increases monotonically in the twofold-degenerate C-type AF $[(0, \pi, \pi)/(\pi, 0, \pi)]$ phase. The qualitative scenario remains the same for $t_z = 1.5$, as shown in Fig. 9(b).

While the analysis of the isotropic NNN hopping case effectively demonstrates that large out-of-plane NN hopping ($t_z > t_x$) fundamentally reshapes the magnetic competition, it does not by itself identify which NNN hopping channel is responsible for this restructuring. In particular, large t_z removes the C-type AF $(\pi, \pi, 0)$ phase and stabilizes the twofold-degenerate C-type AF $[(0, \pi, \pi)/(\pi, 0, \pi)]$ order at large t' , but it remains unclear whether this behavior is driven by the out-of-plane NNN hopping t'_\perp or by the in-plane NNN hopping t'_{xy} . To disentangle these effects, we selectively remove the in-plane NNN hopping ($t'_{xy} = 0$) and analyze the regime where only the out-of-plane NNN hopping, t'_\perp , competes with the dominant out-of-plane NN hopping. Upon switching off the in-plane NNN hopping [see Fig. 9(c)], the twofold-degenerate C-type AF $[(0, \pi, \pi)/(\pi, 0, \pi)]$ phase is completely suppressed, and an A-type AF $(0, 0, \pi)$ insulating state is stabilized instead at large t'_\perp . This shift is physically intuitive: the large t_z favors AF alignment between NNs along the z direction, and a large t'_\perp also promotes AF alignment between NNNs along z . The resulting A-type AF $(0, 0, \pi)$ order accommodates both tendencies simultaneously, as spins are ferromagnetically aligned within each xy plane but alternate antiferromagnetically between adjacent planes. In this specific configuration, both out-of-plane NN and NNN bonds are antiferromagnetically satisfied, making the A-type AF $(0, 0, \pi)$ phase the energetically optimal solution in this regime. Notably, the G-type AF phase is also stabilized over a wider t'_\perp range compared to the preceding isotropic case in Fig. 9(a).

For $t'_{xy} = 0.5$ [see Fig. 9(d)], the resulting phase diagram is significantly richer. The system exhibits a sequential transition: the G-type AF phase persists up to intermediate values of t'_\perp , followed by a narrow window of

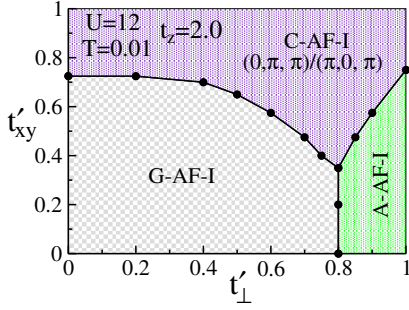


FIG. 10. The t'_\perp - t'_{xy} phase diagram at $T = 0.01$ for $t_z = 2.0$ (representing tensile strain). For small t'_{xy} , the ground state consists of G-type AF insulating state at small to moderate t'_\perp , followed by an A-type AF($0, 0, \pi$) insulating state at sufficiently large t'_\perp ($\gtrsim 0.8$). As t'_{xy} increases, in-plane frustration stabilizes a twofold-degenerate C-type AF[$(0, \pi, \pi)/(\pi, 0, \pi)$] phase over a broad parameter region.

the twofold-degenerate C-type AF[$(0, \pi, \pi)/(\pi, 0, \pi)$] order, and finally transitioning to the A-type AF($0, 0, \pi$) phase at large t'_\perp . Within this complex landscape, T_N exhibits a non-monotonic trend in the C-type AF region, while it continues to decrease for G-type AF and increase for A-type AF, indicating subtle competition between the different NNN couplings. The emergence of the degenerate C-type AF[$(0, \pi, \pi)/(\pi, 0, \pi)$] region is key, as it highlights the interplay of competing exchange channels: the presence of finite t'_{xy} introduces in-plane frustration that destabilizes the G-type AF state and promotes this intermediate C-type AF phase. Thus, the resulting phase sequence arises from two simultaneous competitions: first, the interplay between the out-of-plane NN (t_z) and NNN (t'_\perp) hopping, and second, the balance between the in-plane NN ($t_x = t_y$) and NNN (t'_{xy}) hopping. Crucially, these calculations demonstrate that the in-plane NNN hopping (t'_{xy}) plays a decisive role in stabilizing and modulating the magnetic orders across the phase space.

Next, we present the t'_\perp - t'_{xy} phase diagram in Fig. 10, which clearly demonstrates that the complex emergence and competition of magnetic phases primarily occurs when the in-plane NNN hopping is significant ($t'_{xy} \gtrsim 0.35$). Notably, beyond a high value of t'_{xy} (~ 0.75), the twofold-degenerate C-type AF[$(0, \pi, \pi)/(\pi, 0, \pi)$] phase dominates the ground state, irrespective of the value of the out-of-plane NNN hopping, t'_\perp . It is important to note that such high t'_{xy} values may not be physically viable in real systems. Taken together, our calculations demonstrate that under tensile strain ($t_z = 2$), the dominance of out-of-plane NN hopping qualitatively reshapes the magnetic competition, leading to the emergence of distinct G-type, C-type, and A-type AF regimes, with the aid of t'_{xy} and t'_\perp , that were absent in the compressive limit (e.g., the $t_z = 0.5$ case).

Finally, for completeness, we analyze the low-temperature phase behavior over $0 \leq t_z \leq 2$ to present a unified understanding of how magnetic states evolve across the entire range of hopping, from compressive

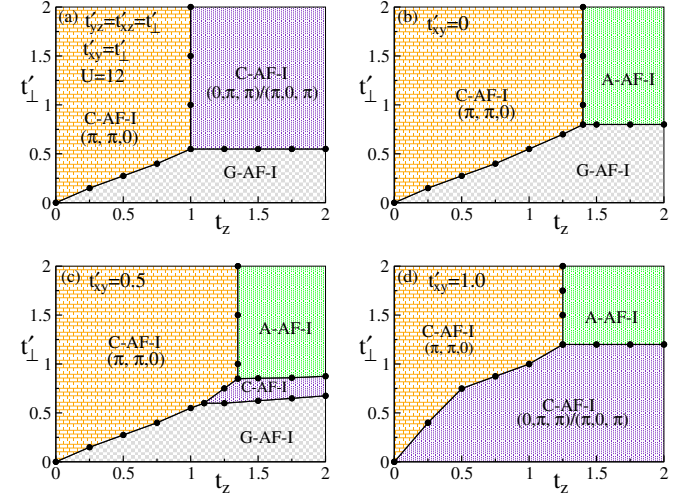


FIG. 11. The t_z - t'_\perp phase diagrams at $T = 0.01$ for various t'_{xy} , illustrating the evolution of magnetic ground states from the compressive ($t_z < t_x$) to tensile ($t_z > t_x$) strain regimes. (a) Isotropic NNN hopping ($t'_{xy} = t'_\perp$): increasing t'_\perp (i.e., t' in this case) drives a transition from the G-type AF phase to a C-type AF phase for all t_z . For $t_z < 1$, the C-type AF($\pi, \pi, 0$) state is stabilized with a critical t'_\perp that increases linearly with t_z . For $t_z > 1$, the system favors a doubly degenerate C-type AF[$(0, \pi, \pi)/(\pi, 0, \pi)$] phase with a nearly constant critical t'_\perp . At $t_z = 1$, cubic symmetry is restored, and the G-type AF insulating phase transitions to a threefold-degenerate C-type AF[$(\pi, \pi, 0)/(0, \pi, \pi)/(\pi, 0, \pi)$] insulating state for $t'_\perp \gtrsim 0.55$. (b) Anisotropic NNN hopping with $t'_{xy} = 0$: the critical out-of-plane hopping t'_\perp required for the G-type AF to C-type AF($\pi, \pi, 0$) transition increases with t_z up to $t_z \sim 1.4$, beyond which an A-type AF($0, 0, \pi$) phase is stabilized at larger t'_\perp . (c) Moderate in-plane NNN hopping ($t'_{xy} = 0.5$): the low- t_z behavior is similar to that in (b); however, in the tensile strain regime, the G-type AF phase gives way first to the doubly degenerate C-type AF[$(0, \pi, \pi)/(\pi, 0, \pi)$] phase and subsequently to the A-type AF($0, 0, \pi$) phase at larger t'_\perp . (d) Large in-plane NNN hopping ($t'_{xy} = 1$): the doubly degenerate C-type AF[$(0, \pi, \pi)/(\pi, 0, \pi)$] phase dominates the phase diagram, suppressing the G-type AF region and significantly reducing the stability of the A-type AF($0, 0, \pi$) phase.

($t_z < t_x$) to tensile ($t_z > t_x$) strain in Fig. 11. While $0 \leq t_z \leq 1$ was previously discussed, the full range is presented here for a detailed comparison across all magnetic phase transitions. The resulting low-temperature t_z - t'_\perp phase diagram, where NNN hoppings are isotropic ($t'_{xy} = t'_\perp = t'$), is presented in Fig. 11(a). For any t_z , increasing t'_\perp , a transition from the G-type AF insulator to the C-type AF insulator is driven, as discussed earlier. Specifically, for $t_z < 1$, this C-type phase is the AF($\pi, \pi, 0$), and the critical t'_\perp value increases linearly with t_z . Conversely, for $t_z > 1$, the phase shifts to a doubly degenerate C-type AF[$(0, \pi, \pi)/(\pi, 0, \pi)$] state, and the critical t'_\perp value remains nearly constant. For $t_z = 1$, the G-type AF order transitions to a threefold degenerate C-type AF[$(0, \pi, \pi)/(\pi, 0, \pi)/(\pi, 0, \pi)$] phase for $t'_\perp \gtrsim 0.55$, due to the restoration of cubic symmetry

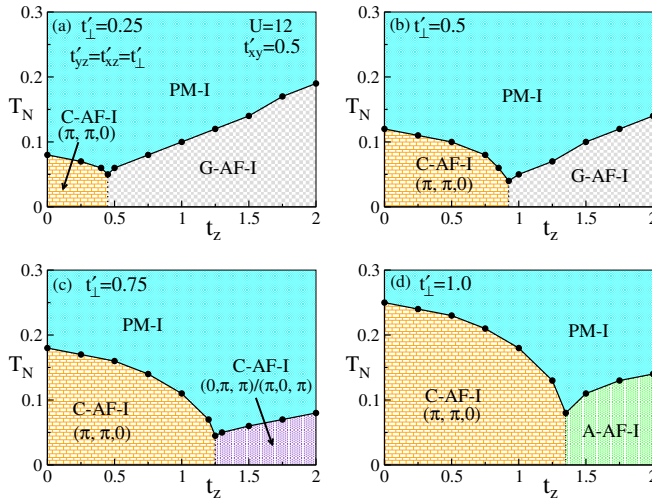


FIG. 12. The t_z - T_N phase diagrams for fixed in-plane NNN hopping $t'_{xy} = 0.5$ at various out-of-plane hoppings: (a) $t'_\perp = 0.25$, (b) $t'_\perp = 0.5$, (c) $t'_\perp = 0.75$, and (d) $t'_\perp = 1.0$. For small-to-moderate t'_\perp (0.25 and 0.5), a C-type AF($\pi, \pi, 0$) phase is stabilized at low t_z ; its T_N decreases as t_z increases until a transition to the G-type AF phase occurs near $t_z \sim 2t'_\perp$. At $t'_\perp = 0.75$, the G-type AF phase is suppressed at large t_z , giving way to a twofold-degenerate C-type AF[$(0, \pi, \pi)/(\pi, 0, \pi)$] phase for $t_z \gtrsim 1.25$. In the large-hopping regime ($t'_\perp = 1.0$), an A-type AF($0, 0, \pi$) phase emerges beyond $t_z \approx 1.35$. In panels (c) and (d), T_N also decreases with t_z within the initial phase and then increases after the magnetic transition into the subsequent phase.

in the NN and NNN hopping.

We next vary the in-plane (t'_{xy}) and out-of-plane (t'_\perp) NNN hopping independently. For $t'_{xy} = 0$ [see Fig. 11(b)], as t_z increases, the critical t'_\perp value required for the G-type to C-type transition increases linearly up to $t_z \sim 1.4$ (this was up to $t_z = 1$ for isotropic NNN hopping). Beyond $t_z \sim 1.4$, increasing t'_\perp drives a transition from G-type AF to A-type AF($0, 0, \pi$) order, where the critical t'_\perp value remains nearly constant. Adding moderate in-plane frustration with $t'_{xy} = 0.5$ [see Fig. 11(c)] preserves the low- t_z behavior but modifies the high- t_z regime. Here, the G-type AF phase first transitions into the doubly degenerate C-type AF[$(0, \pi, \pi)/(\pi, 0, \pi)$] state, before transforming to the A-type AF($0, 0, \pi$) phase at larger t'_\perp , covering almost the whole tensile regime. To complete our ground state analysis of NNN hopping anisotropy, we present the results for large in-plane NNN hopping ($t'_{xy} = 1$) in Fig. 11(d). Here, the doubly degenerate C-type AF[$(0, \pi, \pi)/(\pi, 0, \pi)$] phase dominates a large portion of the phase diagram compared to the $t'_{xy} = 0.5$ case, effectively suppressing the entire G-type AF ordering region and part of the A-type AF($0, 0, \pi$) phase.

Finally, we present the evolution of the T_N as a function of the out-of-plane NN hopping t_z for different out-of-plane NNN hoppings t'_\perp , while fixing $t'_{xy} = 0.5$. This analysis complements the low-temperature phase diagram discussed in Fig. 11(c), which comprises all possible

phases. For small and intermediate t'_\perp values [Figs. 12(a) and (b)], the T_N of the C-type AF($\pi, \pi, 0$) phase decreases with increasing t_z until it transitions to a G-type AF phase around $t_z \sim 2t'_\perp$. Upon further enhancing t'_\perp to 0.75, the G-type AF phase is no longer stable at high t_z values; instead, the twofold-degenerate C-type AF[$((0, \pi, \pi)/(\pi, 0, \pi))$] phase becomes stabilized (beyond $t_z \approx 1.25$), as shown in Fig. 12(c). For a strong NNN hopping, $t'_\perp = 1$ [see Fig. 12(d)], the magnetic behavior is qualitatively distinct: the PM-I state evolves into the C-type AF($\pi, \pi, 0$) phase below $t_z \sim 1.35$, but an A-type AF($0, 0, \pi$) phase emerges above this threshold. Notably, in all cases, the T_N decreases monotonically with t_z until the magnetic transition, after which it increases. Crucially, the T_{MIT} consistently surpasses T_N , which ensures the existence of a stable PM-I regime at finite temperatures above the magnetically ordered phases.

VI. CONCLUSIONS

We investigated the control of magnetic properties and competing AF phases in correlated electron systems by taking BiFeO₃ as model system using epitaxial strain as the tuning parameter. By combining first-principles DFT calculations with s-MC simulations on an anisotropic Hubbard model, we demonstrated a direct microscopic link between strain-induced structural distortion and magnetic phase transitions. Our DFT analysis first identified a direct microscopic link: it revealed that the compressive epitaxial strain induces a structural distortion in BiFeO₃ that drives a transition from the G-type AF phase to a C-type AF($\pi, \pi, 0$) phase by introducing significant anisotropy in exchange interactions. Subsequently, the s-MC phase diagrams, which simulate the effect of strain through anisotropic hopping parameters (t_z and t'_\perp) informed by the DFT analysis, corroborate this G-type to C-type crossover and demonstrate that the in-plane NNN hopping t'_{xy} plays no dominant role in driving this transition. Furthermore, the s-MC calculations predict that tensile strain reorganizes the AF phase landscape, ultimately stabilizing an A-type AF($0, 0, \pi$) phase as well as a twofold-degenerate C-type AF[$((0, \pi, \pi)/(\pi, 0, \pi))$] phase. This integrated study thus established a mechanism where epitaxial strain, by governing directional hopping anisotropies, acts as a potent parameter for engineering competing AF states, leading to a near-degeneracy of multiple AF phases that holds promise for tunable magnetic phase transitions in magnetoelectric and spintronic applications.

ACKNOWLEDGMENT

We acknowledge use of the Meghnad2019 computer cluster at SINP.

Appendix A: Derivation of the Effective Spin-Fermion Hamiltonian

To implement the s-MC framework, we begin by reformulating the quartic on-site interaction term in the Hubbard Hamiltonian [in Eq. 2] using the Hubbard–Stratonovich transformation. This decoupling introduces auxiliary fields that facilitate a tractable quadratic form. First, we express the on-site interaction term as:

$$n_{i,\uparrow}n_{i,\downarrow} = \frac{1}{4}n_i^2 - S_{iz}^2 = \frac{1}{4}n_i^2 - \left(\mathbf{S}_i \cdot \hat{\Omega}_i\right)^2, \quad (\text{A1})$$

where $\mathbf{S}_i = \frac{1}{2} \sum_{\alpha\beta} c_{i,\alpha}^\dagger \boldsymbol{\sigma}_{\alpha\beta} c_{i,\beta}$ is the spin operator at site i (with $\hbar = 1$), and $\boldsymbol{\sigma}$ denotes the Pauli matrices. The arbitrary unit vector $\hat{\Omega}_i$ appears due to SU(2) symmetry, allowing rotational invariance: $S_{ix}^2 = S_{iy}^2 = S_{iz}^2 = (\mathbf{S}_i \cdot \hat{\Omega}_i)^2$ for any $\hat{\Omega}_i$.

The partition function for the Hamiltonian stated in Eq. 2 is defined as $Z = \text{Tr}[e^{-\beta H}]$, with the trace taken over the all particle numbers and site occupations. The inverse temperature is $\beta = 1/T$, and we set $k_B = 1$. To evaluate Z numerically, we discretize the imaginary time interval $[0, \beta]$ into M steps of width $\Delta\tau$ such that $\beta = M\Delta\tau$, and apply a first-order Suzuki–Trotter decomposition:

$$e^{-\beta(H_0+H_I)} \approx (e^{-\Delta\tau H_0} e^{-\Delta\tau H_I})^M + \mathcal{O}(\Delta\tau^2). \quad (\text{A2})$$

Using Eq. A1, the interaction term at a single time slice l can be decoupled into a path integral over scalar and vector auxiliary fields:

$$\int d\phi_i(l) d\Delta_i(l) d^2\Omega_i(l) \exp \left[-\Delta\tau \sum_i \left\{ \frac{\phi_i^2(l)}{U} + i\phi_i(l)n_i + \frac{\Delta_i^2(l)}{U} - 2\Delta_i(l)\hat{\Omega}_i(l) \cdot \mathbf{S}_i \right\} \right], \quad (\text{A3})$$

where $\phi_i(l)$ and $\Delta_i(l)$ are the auxiliary fields for charge and spin density, respectively. We define a vector auxiliary field $\mathbf{m}_i(l) = \Delta_i(l)\hat{\Omega}_i(l)$ to simplify notation. The full partition function becomes:

$$Z \propto \text{Tr} \prod_{l=M}^1 \int d\phi_i(l) d^3\mathbf{m}_i(l) \exp \left[-\Delta\tau \left\{ H_0 + \sum_i \left(\frac{\phi_i^2(l)}{U} + i\phi_i(l)n_i + \frac{\mathbf{m}_i^2(l)}{U} - 2\mathbf{m}_i(l) \cdot \mathbf{S}_i \right) \right\} \right]. \quad (\text{A4})$$

At this stage, the formulation is exact, preserving full SU(2) spin symmetry, with auxiliary fields depending on both space and imaginary time.

To make the problem computationally feasible within the s-MC approach, we adopt two approximations: (i) we drop the imaginary-time dependence of the auxiliary fields, treating ϕ_i and \mathbf{m}_i as classical fields; and (ii) we fix the charge field to its saddle-point value, $i\phi_i = \frac{U}{2}\langle n_i \rangle$.

With a rescaling $\mathbf{m}_i \rightarrow \frac{U}{2}\mathbf{m}_i$, we obtain the following effective Hamiltonian:

$$H_{\text{eff}} = -t \sum_{\langle i,j \rangle, \sigma} c_{i,\sigma}^\dagger c_{j,\sigma} - t' \sum_{\langle\langle i,j \rangle\rangle, \sigma} c_{i,\sigma}^\dagger c_{j,\sigma} + \frac{U}{2} \sum_i (\langle n_i \rangle n_i - \mathbf{m}_i \cdot \boldsymbol{\sigma}_i) + \frac{U}{4} \sum_i (\mathbf{m}_i^2 - \langle n_i \rangle^2) - \mu \sum_i n_i, \quad (\text{A5})$$

as presented earlier in Eq. 3. The resulting spin-fermion model describes itinerant electrons interacting with classical auxiliary fields $\{\mathbf{m}_i\}$, which are sampled using Monte Carlo techniques.

Appendix B: Definitions of Physical Observables

To characterize the magnetic and transport properties of the system, we compute several observables, including the magnetic structure factor, local magnetic moment, specific heat, density of states, and resistivity. These quantities serve as key indicators of phase transitions and ordering tendencies within the spin-fermion model governed by Eq. 3.

Magnetic correlations: The magnetic ordering is quantified using the spin structure factor $S(\mathbf{q})$, which captures long-range spin correlations. It is defined as

$$S(\mathbf{q}) = \frac{1}{(L^3)^2} \sum_{k,l} \langle \mathbf{S}_k \cdot \mathbf{S}_l \rangle e^{-i\mathbf{q} \cdot (\mathbf{r}_k - \mathbf{r}_l)}, \quad (\text{B1})$$

which is measured in units of \hbar^2 . \mathbf{S}_k denotes the spin operator at site k , and the angular brackets indicate combined quantum and thermal averages. The sum runs over all pairs of lattice sites on a system of volume L^3 , where L is the length of the sides of the simple cubic lattice. Specific wave vectors \mathbf{q} correspond to distinct magnetic configurations (for detail see Fig. 1): $\mathbf{q} = (\pi, \pi, \pi)$ indicates G-type AF phase; $\mathbf{q} = (\pi, \pi, 0), (0, \pi, \pi), (\pi, 0, \pi)$ denote C-type AF orders; while $\mathbf{q} = (0, 0, \pi), (\pi, 0, 0), (0, \pi, 0)$ signal A-type AF alignment.

Local moment: The local magnetic moment M is defined as the average of the square of quantum magnetization:

$$M = \langle (n_\uparrow - n_\downarrow)^2 \rangle = \langle n \rangle - 2\langle n_\uparrow n_\downarrow \rangle, \quad (\text{B2})$$

with units of \hbar^2 . $\langle n \rangle = \langle n_\uparrow + n_\downarrow \rangle$ is the average electron density of the system. At half-filling ($\langle n \rangle = 1$), the moment is bounded between $M = 0.5$ (uncorrelated or high-temperature limit) and $M = 1$ (large coupling $U \rightarrow \infty$, where double occupancy vanishes). Thus, the evolution of M with temperature and interaction strength provides insight into local moment formation.

Specific heat: The specific heat C_v is computed as the derivative of the total energy with respect to temper-

ature (central difference method is used for the derivative):

$$C_v = \frac{dE}{dT}. \quad (\text{B3})$$

Here, E includes contributions from both fermionic degrees of freedom (quantum energy) and the classical auxiliary fields (classical energy). Numerically, we evaluate C_v using central difference scheme.

Density of states: To probe the electronic spectrum, we calculate the DOS, defined as

$$N(\omega) = \sum_{i=1}^{2L^3} \delta(\omega - \omega_i), \quad (\text{B4})$$

where ω_i are the eigenvalues of the effective Hamiltonian in Eq. 3. In practice, the δ -function is replaced by a Lorentzian with a broadening of $\sim W/(2L^3)$, where W denotes the bandwidth of the noninteracting model. The factor $2L^3$ corresponds to the total number of single-particle states. The Fermi energy is taken to be $\omega = 0$ in all spectral analyses.

Resistivity: Transport properties are evaluated via the *dc* limit of the optical conductivity, which is computed using the Kubo-Greenwood formula [95, 97]:

$$\sigma_z(\omega) = \frac{\pi e^2}{L^3 \hbar a_0} \sum_{\alpha, \beta} (n_\alpha - n_\beta) \frac{|f_{\alpha\beta}^z|^2}{\omega_\beta - \omega_\alpha} \delta(\omega - (\omega_\beta - \omega_\alpha)), \quad (\text{B5})$$

where a_0 is the lattice parameter and we have expressed σ_z in units of $\frac{e^2}{\hbar a_0}$. $n_\alpha = f(\mu - \omega_\alpha)$ is the Fermi-Dirac distribution and $f_{\alpha\beta}^z = \langle \psi_\alpha | J_z | \psi_\beta \rangle$ denotes the current matrix element along the z direction. The current operator along the z direction is defined as

$$\begin{aligned} J_z = ia_0 \sum_{i, \sigma} & t_z (c_{i, \sigma}^\dagger c_{i+a_0 \hat{z}, \sigma} - \text{H.c.}) \\ & + t'_{xz} (c_{i, \sigma}^\dagger c_{i+a_0 \hat{z}+a_0 \hat{x}, \sigma} - \text{H.c.}) \\ & + t'_{yz} (c_{i, \sigma}^\dagger c_{i+a_0 \hat{z}+a_0 \hat{y}, \sigma} - \text{H.c.}). \end{aligned}$$

The eigenvalues ω_α and corresponding eigenstates ψ_α are obtained from diagonalizing H_{eff} . The *dc* conductivity (along the z -axis) σ_{dc}^z is estimated by integrating $\sigma_z(\omega)$ over a small low-frequency interval:

$$\sigma_{\text{dc}}^z = \frac{1}{\Delta\omega} \int_0^{\Delta\omega} \sigma_z(\omega) d\omega. \quad (\text{B6})$$

The parameter $\Delta\omega$ is chosen to be approximately four to five times larger than the system's average finite-size gap, which is estimated as the total bandwidth divided by the number of eigenvalues. The resistivity along the z direction is defined as $\rho_z = 1/\sigma_{\text{dc}}^z$.

[1] E. Dagotto, Complexity in strongly correlated electronic systems, *Science* **309**, 257 (2005).

[2] E. Dagotto and Y. Tokura, Strongly correlated electronic materials: Present and future, *MRS Bull.* **33**, 1037 (2008).

[3] *Strongly Correlated Systems*, edited by A. Avella and F. Mancini (Springer, Berlin, 2014).

[4] M. Liu, A. J. Sternbach, and D. N. Basov, Nanoscale electrodynamics of strongly correlated quantum materials, *Rep. Prog. Phys.* **80**, 014501 (2016).

[5] S. Sachdev, Quantum magnetism and criticality, *Nat. Phys.* **4**, 173–185 (2008).

[6] C. Lacroix, P. Mendels, and F. Mila (Eds.), *Introduction to Frustrated Magnetism* (Springer, Berlin, 2011).

[7] S. Sachdev, *Quantum Phases of Matter* (Cambridge University Press, 2023).

[8] E. Y. Tsymbal, E. R. A. Dagotto, C.-B. Eom, and R. Ramesh, *Multifunctional Oxide Heterostructures*, (Oxford University Press, Oxford, 2012).

[9] S. B. Lee, R. K. Kaul, and L. Balents, Interplay of quantum criticality and geometric frustration in columbite, *Nat. Phys.* **6**, 702–706 (2010).

[10] M. Hanbucken and J.-P. Deville (Eds.), *Stress and Strain in Epitaxy* (Elsevier Science, 2001).

[11] M. Zhong (Ed.), *Epitaxy* (IntechOpen, 2018).

[12] K. Dutta and R. Singh, Magnetoelastic coupling and critical behavior of some strongly correlated magnetic systems, *J. Phys.: Condens. Matter* **35**, 083001 (2022).

[13] S. B. Roy, First order magneto-structural phase transition and associated multi-functional properties in magnetic solids, *J. Phys.: Condens. Matter* **25**, 183201 (2013).

[14] H. Yan, Z. Feng, S. Shang, X. Wang, Z. Hu, J. Wang, Z. Zhu, H. Wang, Z. Chen, H. Hua, W. Lu, J. Wang, P. Qin, H. Guo, X. Zhou, Z. Leng, Z. Liu, C. Jiang, M. Coey, and Z. Liu, A piezoelectric, strain-controlled antiferromagnetic memory insensitive to magnetic fields, *Nat. Nanotechnol.* **14**, 131–136 (2019).

[15] M. Imada, A. Fujimori, and Y. Tokura, Metal-insulator transitions, *Rev. Mod. Phys.* **70**, 1039–1263 (1998).

[16] Y. Tokura, Critical features of colossal magnetoresistive manganites, *Rep. Prog. Phys.* **69**, 797 (2006).

[17] E. Dagotto, T. Hotta, and A. Moreo, Colossal magnetoresistive materials: the key role of phase separation, *Phys. Rep.* **344**, 1–153 (2001).

[18] J.-S. Zhou and J. B. Goodenough, Intrinsic structural distortion in orthorhombic perovskite oxides, *Phys. Rev. B* **77**, 132104 (2008).

[19] C. J. Bartel, C. Sutton, B. R. Goldsmith, R. Ouyang, C. B. Musgrave, L. M. Ghiringhelli, and M. Scheffler, New tolerance factor to predict the stability of perovskite oxides and halides, *Sci. Adv.* **5**, eaav0693 (2019).

[20] H. Somaly, S. Kolesnik, J. Mais, D. Brown, K. Chapagain, B. Dabrowski, and O. Chmaissem, Strain-induced tetragonal distortions and multiferroic properties in polycrystalline $\text{Sr}_{1-x}\text{Ba}_x\text{MnO}_3$ ($x = 0.43\text{--}0.45$) perovskites, *Phys. Rev. Mater.* **2**, 054408 (2018).

[21] H. Chen and A. J. Millis, Phase diagram of $\text{Sr}_{1-x}\text{Ba}_x\text{MnO}_3$ as a function of chemical doping, epitaxial strain, and external pressure, *Phys. Rev. B* **94**, 165106 (2016).

[22] R. Bindu, K. Maiti, R. Rawat, and S. Khalid, Electronic and structural transition in $\text{La}_{0.2}\text{Sr}_{0.8}\text{MnO}_3$, *Appl. Phys. Lett.* **92**, 121906 (2008).

[23] L. Pinsard, J. Rodríguez-Carvajal, and A. Revcolevschi, Structural phase diagram of $\text{La}_{1-x}\text{Sr}_x\text{MnO}_3$ for low Sr doping, *J. Alloys Compd.* **262**–**263**, 152–156 (1997).

[24] S. K. Chaluvadi, V. Polewczyk, A. Yu. Petrov, G. Vinai, L. Braglia, J. M. Diez, V. Pierron, P. Perna, L. Mechini, P. Torelli, and P. Orgiani, Electronic properties of fully strained $\text{La}_{1-x}\text{Sr}_x\text{MnO}_3$ thin films grown by molecular beam epitaxy ($0.15 \leq x \leq 0.45$), *ACS Omega* **7**, 14571–14578 (2022).

[25] P. Sharma, S. Pathak, H. Pant, and R. Bindu, Strain induced phase transition in $\text{La}_{0.2}\text{Sr}_{0.8}\text{MnO}_3$, *Appl. Phys. A* **128**, 271 (2022).

[26] Z. Zeng, M. Greenblatt, and M. Croft, Large magnetoresistance in antiferromagnetic $\text{CaMnO}_{3-\delta}$, *Phys. Rev. B* **59**, 8784–8788 (1999).

[27] Y. Kawazoe, T. Kanomata, and R. Note, *High Pressure Materials Properties: Magnetic Properties of Oxides Under Pressure: A Supplement to Landolt-Börnstein IV/22 Series*, (Springer, Berlin, Heidelberg, 2023).

[28] Y. Xu, Z. Tan, W.-T. Chen, C.-K. Chang, Y.-C. Chuang, M. Goto, and Y. Shimakawa, High-pressure synthesized perovskite CdMnO_3 with C-type antiferromagnetic spin configuration, *Inorg. Chem.* **61**, 21011–21015 (2022).

[29] I. Bersuker, *The Jahn-Teller Effect* (Cambridge University Press, Cambridge, 2006).

[30] H. Koppel, D. Yarkony, and H. Barentzen (Eds.), *The Jahn-Teller Effect* (Springer Berlin, Heidelberg, 2009).

[31] S. V. Streltsov and D. I. Khomskii, Jahn-Teller Effect and Spin-Orbit Coupling: Friends or Foes?, *Phys. Rev. X* **10**, 031043 (2020).

[32] T. Hotta, S. Yunoki, M. Mayr, and E. Dagotto, A-type antiferromagnetic and C-type orbital-ordered states in LaMnO_3 using cooperative Jahn-Teller phonons, *Phys. Rev. B* **60**, R15009 (1999).

[33] Y. Kobayashi, T. Mitsunaga, G. Fujinawa, T. Arii, M. Suetake, K. Asai, and J. Harada, Structural phase transition from rhombohedral to cubic in LaCoO_3 , *J. Phys. Soc. Jpn.* **69**, 3468 (2000).

[34] G. P. Carman and N. Sun, Strain-mediated magnetoelectrics: Turning science fiction into reality, *MRS Bull.* **43**, 822 (2018).

[35] D. Bhattacharya, S. Bandyopadhyay, and J. Atulasimha, Review: Voltage induced strain control of magnetization: computing and other applications, *Multifunct. Mater.* **2**, 032001 (2019).

[36] S. Bandyopadhyay, J. Atulasimha, and A. Barman, Magnetic straintronics: Manipulating the magnetization of magnetostriuctive nanomagnets with strain for energy-efficient applications, *Appl. Phys. Rev.* **8**, 041323 (2021).

[37] Y. Qi, M. A. Sadi, D. Hu, M. Zheng, Z. Wu, Y. Jiang, and Y. P. Chen, Recent Progress in Strain Engineering on Van der Waals 2D Materials: Tunable Electrical, Electrochemical, Magnetic, and Optical Properties, *Adv. Mater.* **35**, 2205714 (2023).

[38] A. Bhattacharya and S. J. May, Magnetic Oxide Heterostructures, *Annu. Rev. Mater. Res.* **44**, 65 (2014).

[39] S. Dhole, A. Chen, W. Nie, B. Park, and Q. Jia, Strain Engineering: A Pathway for Tunable Functionalities of Perovskite Metal Oxide Films, *Nanomaterials* **12**, 835 (2022).

[40] A. Sarkar, R. Kruk, and H. Hahn, Magnetic properties of high entropy oxides, *Dalton Trans.* **50**, 1973–1982 (2021).

[41] A. Vailionis, H. Boschker, W. Siemons, E. P. Houwman, D. H. A. Blank, G. Rijnders, and G. Koster, Misfit strain accommodation in epitaxial ABO_3 perovskites: Lattice rotations and lattice modulations, *Phys. Rev. B* **83**, 064101 (2011).

[42] M. Mirjolet, H. B. Vasili, A. Valadkhani, J. Santiso, V. Borisov, P. Gargiani, M. Valvidares, R. Valentí, and J. Fontcuberta, Orbital occupancy and hybridization in strained SrVO_3 epitaxial films, *Phys. Rev. Mater.* **5**, 095002 (2021).

[43] Y. Li, X. Yang, H. Bai, M. Wang, D. Cheng, C. Song, Z. Yuan, Y. Liu, and Z. Shi, Strain-tunable magnetic compensation temperature of epitaxial $\text{Tb}_3\text{Fe}_5\text{O}_{12}$ thin films, *Phys. Rev. B* **108**, 184403 (2023).

[44] E.-J. Guo, R. Desautels, D. Keavney, M. A. Roldan, B. J. Kirby, D. Lee, Z. Liao, T. Charlton, A. Herklotz, T. Z. Ward, M. R. Fitzsimmons, and H. N. Lee, Nanoscale ferroelastic twins formed in strained LaCoO_3 films, *Sci. Adv.* **5**, eaav5050 (2019).

[45] E. Paris, Y. Tseng, E. M. Pärschke, W. Zhang, M. H. Upton, A. Efimenko, K. Rolfs, D. E. McNally, L. Maurel, M. Naamneh, M. Caputo, V. N. Strocov, Z. Wang, D. Casa, C. W. Schneider, E. Pomjakushina, K. Wohlfeld, M. Radović, and T. Schmitt, Strain engineering of the charge and spin-orbital interactions in Sr_2IrO_4 , *Proc. Natl. Acad. Sci. U.S.A.* **117**, 24764 (2020).

[46] Y. K. Wakabayashi, S. Kaneta-Takada, Y. Krockenberger, Y. Taniyasu, and H. Yamamoto, Wide-range epitaxial strain control of electrical and magnetic properties in high-quality SrRuO_3 films, *ACS Appl. Electron. Mater.* **3**, 2712 (2021).

[47] C. Lupo, E. Sheridan, E. Fertitta, D. Dubbink, C. J. Pickard, and C. Weber, From Slater to Mott physics by epitaxially engineering electronic correlations in oxide interfaces, *npj Comput. Mater.* **7**, 94 (2021).

[48] S. Mo, T. Katayama, A. Chikamatsu, M. Kitamura, K. Horiba, H. Kumigashira, and T. Hasegawa, Epitaxial-Strain-Induced Spontaneous Magnetization in Polar $\text{Mn}_2\text{Mo}_3\text{O}_8$, *Chem. Mater.* **33**, 7713–7718 (2021).

[49] B. Paudel, Y. Sharma, B. K. Derby, G. Pilania, M. M. Schneider, A. C. Jones, H. Nakotte, M. T. Pettes, and A. Chen, Effect of lattice strain on magnetism in epitaxial YCrO_3 films, *Mater. Res. Lett.* **10**, 29–35 (2022).

[50] A. Lupascu, J. P. Clancy, H. Gretarsson, Z. Nie, J. Nichols, J. Terzic, G. Cao, S. S. A. Seo, Z. Islam, M. H. Upton, J. Kim, D. Casa, T. Gog, A. H. Said, V. M. Katukuri, H. Stoll, L. Hozoi, J. van den Brink, and Y.-J. Kim, Tuning Magnetic Coupling in Sr_2IrO_4 Thin Films with Epitaxial Strain, *Phys. Rev. Lett.* **112**, 147201 (2014).

[51] A. Seo, P. P. Stavropoulos, H.-H. Kim, K. Fürsich, M. Souri, J. G. Connell, H. Gretarsson, M. Minola, H. Y. Kee, and B. Keimer, Compressive strain induced enhancement of exchange interaction and short-range

magnetic order in Sr_2IrO_4 investigated by Raman spectroscopy, *Phys. Rev. B* **100**, 165106 (2019).

[52] H. Banerjee, Understanding the role of exchange and correlations in complex oxides under strain and oxide heterostructures, *Mod. Phys. Lett. B* **34**, 2030006 (2020).

[53] D. S. Tsvetkov, V. V. Sereda, D. A. Malyshkin, I. L. Ivanov, and A. Yu. Zuev, Chemical lattice strain in non-stoichiometric oxides: an overview, *J. Mater. Chem. A* **10**, 6351–6375 (2022).

[54] B. J. Kim, H. Ohsumi, T. Komesu, S. Sakai, T. Morita, H. Takagi, and T. Arima, Phase-Sensitive Observation of a Spin-Orbital Mott State in Sr_2IrO_4 , *Science* **323**, 1329–1332 (2009).

[55] J. Nichols, J. Terzic, E. G. Bittle, O. B. Korneta, L. E. De Long, J. W. Brill, G. Cao, and S. S. A. Seo, Tuning electronic structure via epitaxial strain in Sr_2IrO_4 thin films, *Appl. Phys. Lett.* **102**, 141908 (2013).

[56] S. Geprags, B. E. Skovdal, M. Scheufele, M. Opel, D. Wermeille, P. Thompson, A. Bombardi, V. Simonet, S. Grenier, P. Lejay, G. A. Chahine, D. L. Quintero-Castro, R. Gross, and D. Mannix, Precise control of $J_{\text{eff}} = \frac{1}{2}$ magnetic properties in Sr_2IrO_4 epitaxial thin films by variation of strain and thin film thickness, *Phys. Rev. B* **102**, 214402 (2020).

[57] V. Scagnoli, M. Allieta, H. Walker, M. Scavini, T. Katsumi, L. Sagarna, O. Zaharko, and C. Mazzoli, EuTiO_3 magnetic structure studied by neutron powder diffraction and resonant x-ray scattering, *Phys. Rev. B* **86**, 094432 (2012).

[58] A. Midya, P. Mandal, Km. Rubi, R. Chen, J.-S. Wang, R. Mahendiran, G. Lorusso, and M. Evangelisti, Large adiabatic temperature and magnetic entropy changes in EuTiO_3 , *Phys. Rev. B* **93**, 094422 (2016).

[59] V. V. Laguta, S. Kamba, M. Maryško, B. Andrzejewski, M. Kachlík, K. Maca, J. H. Lee, and D. G. Schlom, Magnetic resonance study of bulk and thin film EuTiO_3 , *J. Phys.: Condens. Matter* **29**, 105401 (2017).

[60] Y. Lin, E.-M. Choi, P. Lu, X. Sun, R. Wu, C. Yun, B. Zhu, H. Wang, W. Li, T. Maity, and J. MacManus-Driscoll, Vertical Strain-Driven Antiferromagnetic to Ferromagnetic Phase Transition in EuTiO_3 Nanocomposite Thin Films, *ACS Appl. Mater. Interfaces* **12**, 8513–8521 (2020).

[61] Z. Fan, J. Wang, M. B. Sullivan, A. Huan, D. J. Singh, and K. P. Ong, Structural Instability of Epitaxial (001) BiFeO_3 Thin Films under Tensile Strain, *Sci. Rep.* **4**, 4631 (2014).

[62] G. J. MacDougall, H. M. Christen, W. Siemons, M. D. Biegalski, J. L. Zarestky, S. Liang, E. Dagotto, and S. E. Nagler, Antiferromagnetic transitions in tetragonal-like BiFeO_3 , *Phys. Rev. B* **85**, 100406 (2012).

[63] H. Dixit, C. Beekman, C. M. Schlepütz, W. Siemons, Y. Yang, N. Senabulya, R. Clarke, M. Chi, H. M. Christen, and V. R. Cooper, Understanding Strain-Induced Phase Transformations in BiFeO_3 Thin Films, *Adv. Sci.* **2**, 1500041 (2015).

[64] Y. Yang, I. C. Infante, B. Dkhil, and L. Bellaiche, Strain effects on multiferroic BiFeO_3 films, *C. R. Phys.* **16**, 193–203 (2015).

[65] S. Goswami, S. Mishra, K. K. Sahoo, B. Kumar, M. R. Sahoo, S. Chatterjee, D. Mukherjee, K. Pradhan, A. Garg, C. K. Ghosh, and D. Bhattacharya, Evidence of spin reorientation transition below 150 K from magnetic force microscopy in a ferromagnetic BiFeO_3 thin film, *Phys. Rev. B* **110**, 214401 (2024).

[66] O. Dieguez and J. Iniguez, First-Principles Investigation of Morphotropic Transitions and Phase-Change Functional Responses in BiFeO_3 - BiCoO_3 Multiferroic Solid Solutions, *Phys. Rev. Lett.* **107**, 057601 (2011).

[67] H.-C. Ding and C.-G. Duan, Electric-field control of magnetic ordering in the tetragonal-like BiFeO_3 , *Europhys. Lett.* **97**, 57007 (2012).

[68] C. Escorihuela-Sayalero, O. Dieguez, and J. Iniguez, Strain Engineering Magnetic Frustration in Perovskite Oxide Thin Films, *Phys. Rev. Lett.* **109**, 247202 (2012).

[69] M. R. Walden, C. V. Ciobanu, and G. L. Brennecke, Density-functional theory calculation of magnetic properties of BiFeO_3 and BiCrO_3 under epitaxial strain, *J. Appl. Phys.* **130**, 104102 (2021).

[70] M. R. Walden, C. V. Ciobanu, and G. L. Brennecke, First-principles indicators of ferroic parameters in epitaxial BiFeO_3 and BiCrO_3 , *J. Appl. Phys.* **132**, 024102 (2022).

[71] W.-Y. Tong, H.-C. Ding, S. J. Gong, X. Wan, and C.-G. Duan, Magnetic ordering induced giant optical property change in tetragonal BiFeO_3 , *Sci. Rep.* **5**, 17993 (2015).

[72] P. C. Rout and U. Schwingenschlögl, Large Spin Coherence Length and High Photovoltaic Efficiency of the Room Temperature Ferrimagnet $\text{Ca}_2\text{FeOsO}_6$ by Strain Engineering, *Adv. Sci.* **9**, 2106037 (2022).

[73] P. C. Rout and U. Schwingenschlögl, Strain-attenuated spin frustration in double perovskite $\text{Sr}_2\text{FeOsO}_6$, *Phys. Rev. B* **103**, 024426 (2021).

[74] F. Andrei, M. Dinescu, V. Ion, F. Craciun, R. Birjega, and N. D. Scarisoreanu, Impact of structural strain in perovskite epitaxial thin films on their functional properties, *Crystals* **13**, 1686 (2023).

[75] M. C. Gutzwiller, Effect of Correlation on the Ferromagnetism of Transition Metals, *Phys. Rev. Lett.* **10**, 159–162 (1963).

[76] J. Kanamori, Electron Correlation and Ferromagnetism of Transition Metals, *Prog. Theor. Phys.* **30**, 275–289 (1963).

[77] J. Hubbard and B. H. Flowers, Electron correlations in narrow energy bands III. An improved solution, *Proc. R. Soc. A* **281**, 401–419 (1964).

[78] R. Staudt, M. Dzierzawa, and A. Muramatsu, Phase diagram of the three-dimensional Hubbard model at half filling, *Eur. Phys. J. B* **17**, 411–415 (2000).

[79] D. P. Arovas, E. Berg, S. A. Kivelson, and S. Raghu, The Hubbard Model, *Annu. Rev. Condens. Matter Phys.* **13**, 239–274 (2022).

[80] M. Qin, T. Schäfer, S. Andergassen, P. Corboz, and E. Gull, The Hubbard Model: A Computational Perspective, *Annu. Rev. Condens. Matter Phys.* **13**, 275–302 (2022).

[81] A. Mukherjee, N. D. Patel, S. Dong, S. Johnston, A. Moreo, and E. Dagotto, Testing the Monte Carlo–mean field approximation in the one-band Hubbard model, *Phys. Rev. B* **90**, 205133 (2014).

[82] G. Jana and A. Mukherjee, Frustration effects at finite temperature in the half-filled Hubbard model, *J. Phys.: Condens. Matter* **32**, 365602 (2020).

[83] S. Chakraborty, A. Mukherjee, and K. Pradhan, Antiferromagnetism beyond the classical percolation threshold in the diluted half-filled one-band Hubbard model in three dimensions, *Phys. Rev. B* **106**, 075146 (2022).

[84] J. K. Bidika, S. Mandal, Y. Shimakawa, K. Pradhan, and

B. R. K. Nanda, Tunable magnetism in spin-half *A*-site ordered perovskites: $\text{CaCu}_3\text{B}_4\text{O}_{12}$, *Phys. Rev. B* **110**, 165161 (2024).

[85] S. Halder, S. Mandal, and K. Pradhan, Microscopic study of interlayer magnetic coupling across the interface in antiferromagnetic bilayers, *Phys. Rev. B* **111**, 125149 (2025).

[86] S. Mandal, S. Halder, and K. Pradhan, Exploring the magnetic phases in the one-band Hubbard model: Impact of long-range hopping, *Phys. Rev. B* **112**, 085150 (2025).

[87] S. Mandal, S. Chakraborty, and K. Pradhan, Combined effect of site dilution and long-range interactions in the Hubbard model: Towards the design of antiferromagnetic half-metallicity, *Phys. Rev. B* **112**, 205113 (2025).

[88] G. Kresse and J. Furthmüller, Efficient iterative schemes for ab initio total-energy calculations using a plane-wave basis set, *Phys. Rev. B* **54**, 11169 (1996).

[89] G. Kresse and D. Joubert, From ultrasoft pseudopotentials to the projector augmented-wave method, *Phys. Rev. B* **59**, 1758 (1999).

[90] O. Dieguez, O. E. Gonzalez-Vazquez, J. C. Wojdel, and J. Iñiguez, First-principles predictions of low-energy phases of multiferroic BiFeO_3 , *Phys. Rev. B* **83**, 094105 (2011).

[91] J. P. Perdew, K. Burke, and M. Ernzerhof, Generalized Gradient Approximation Made Simple, *Phys. Rev. Lett.* **77**, 3865 (1996).

[92] S. L. Dudarev, G. A. Botton, S. Y. Savrasov, C. J. Humphreys, and A. P. Sutton, Electron-energy-loss spectra and the structural stability of nickel oxide: An LSDA+U study, *Phys. Rev. B* **57**, 1505–1509 (1998).

[93] M. Laubach, D. G. Joshi, J. Reuther, R. Thomale, M. Vojta, and S. Rachel, Quantum disordered insulating phase in the frustrated cubic-lattice Hubbard model, *Phys. Rev. B* **93**, 041106 (2016).

[94] L. Fratino, M. Charlebois, P. Semon, G. Sordi, and A. M. S. Tremblay, Effects of interaction strength, doping, and frustration on the antiferromagnetic phase of the two-dimensional Hubbard model, *Phys. Rev. B* **96**, 241109 (2017).

[95] S. Kumar and P. Majumdar, A travelling cluster approximation for lattice fermions strongly coupled to classical degrees of freedom, *Eur. Phys. J. B* **50**, 571–579 (2006).

[96] Thereza Paiva, R. T. Scalettar, Carey Huscroft, and A. K. McMahan, Signatures of spin and charge energy scales in the local moment and specific heat of the half-filled two-dimensional Hubbard model, *Phys. Rev. B* **63**, 125116 (2001).

[97] G. D. Mahan, *Many-Particle Physics*, (Springer US, Boston, MA, 2000), pp. 499–577.